A stable microtubule bundle formed through an orchestrated multistep process controls quiescence exit

Damien Laporte[1]*, Aurélie Massoni-Laporte[1], Charles Lefranc[1], Jim Dompierre[1], David Mauboules[1], Emmanuel. T. Nsamba[2], Anne Royou[1], Lihi Gal[3], Maya Schuldiner[3], Mohan L. Gupta Jr[2], Isabelle Sagot[1]

Affiliation :

1: Univ. Bordeaux, CNRS, IBGC, UMR 5095, Bordeaux, France

2: Genetics, Development, and Cell Biology, Iowa State University, Ames, IA 50011, USA.

3: Department of Molecular Genetics, Weizmann Institute of Science, Rehovot, Israel

* Corresponding author: Damien.laporte@ibgc.cnrs.fr

Abstract

Cells fine-tune microtubule assembly in both space and time, to give rise to distinct edifices with specific cellular functions. In proliferating cells, microtubules are highly dynamics, and proliferation cessation often leads to their stabilization. One of the most stable microtubule structures identified to date is the nuclear bundle assembled in quiescent yeast. In this report, we characterize the original multistep process driving the assembly of this structure. This AuroraB-dependent mechanism follows a precise temporality that relies on the sequential actions of kinesin-14, kinesins-5 and involves both microtubule-kinetochore and kinetochore-kinetochore interactions. Upon quiescence exit, the microtubule bundle is disassembled via a cooperative process involving kinesin-8 and its full disassembly is required prior to cells re-entry into proliferation. Overall, our study provides the first description, at the molecular scale, of the entire life cycle of a stable microtubule structure *in vivo*, and sheds light on its physiological function.

Introduction

Microtubules (MTs) are hollow cylindrical polymers assembled by the non-covalent interaction of α- and β-tubulin heterodimers. MTs are generally nucleated at MT organizing centers (MTOC) by a ɣ-tubulin complex (ɣ-TuC) which acts as a template and stabilizes the so-called MT "minus-end" (Liu et al., 2021; Roostalu and Surrey, 2017; Sanchez and Feldman, 2017; Thawani and Petry, 2021). At the opposite end, the "plus-end" (+end), MTs elongate by the addition of GTP tubulin. The β-tubulin bound GTP is hydrolyzed, and stable but transient, GDP + Pi intermediates are generated in the region immediately behind the growing +end. Subsequent Pi release favors MT depolymerization which can be rescued by *de novo* GTP-tubulin addition (Cleary and Hancock, 2021; Gudimchuk and McIntosh, 2021). Thus, MTs alternate between periods of growth and shrinkage, a behavior termed dynamic instability (Mitchison and Kirschner, 1984). *In vivo*, a profusion of MT-associated proteins (MAPs) regulate MT length and dynamics (Bodakuntla et al., 2019; Goodson and Jonasson, 2018). In addition, MTs are often assembled from multiple tubulin variants or isotypes, and are modified by a cohort of post-translational modifications that modulate MT dynamics directly or by influencing the recruitment of MAPs (Janke and Magiera, 2020; Roll-Mecak, 2020). Other MAPs organize MTs into highly-ordered assemblies either by cross-linking MTs or by connecting them with cellular structures such as membranes, chromosomes, or actin cytoskeleton components (Bodakuntla et al., 2019; Meiring et al., 2020). Cells fine-tune these mechanisms in both space and time to give rise to distinct MT edifices with specific functions.

In proliferating cells, MT dynamics are crucial for their functions. It allows exploration of the cell volume in search of structures to "capture", such as centromeres during mitosis, or to exert pushing or pulling forces required for various cellular processes such as cell migration or morphogenesis (Heald and Khodjakov, 2015; Kirschner and Mitchison, 1986). The MT

58 cytoskeleton can undergo extensive rearrangements and assemble more stable MT
59 structures, especially when cells change fate (Meiring et al., 2020; Röper, 2020). For example,
60 in terminally differentiated cells, such as epithelial cells, cardiomyocytes or neurons, stable
61 MT networks make up the majority, and ensure critical cellular functions such as cell shape
62 maintenance or long-distance intracellular transport (Baas et al., 2016; Muroyama and
63 Lechler, 2017). Defects in MT stabilization are at the origin of many human pathologies,
64 including neurodegenerative diseases and ciliopathies (Anvarian et al., 2019; Wheway et al.,
65 2018). Effectors responsible for MT stabilization have been actively searched for since the
66 1980's. In mammals, the involvement of specific MAPs such as Tau, MAP2, MAP6 and PRC1,
67 or tubulin post-translational modifications has been extensively studied. While their
68 contributions to MT stabilization are central and undisputed, their sole actions do not fully
69 explain the observed levels of MT stability in many types of non-dividing cells (Hahn et al.,
70 2019).

71 For years, yeast species have been instrumental in unraveling mechanisms that
72 regulate MT dynamics in eukaryotes. While proliferating yeast cells exhibit a dynamic MT
73 network (Winey and Bloom, 2012), proliferation cessation goes with the formation of
74 dramatically stable MT structures in both *S. cerevisiae* and *S. pombe* (Laporte and Sagot, 2014;
75 Laporte et al., 2013, 2015). Upon quiescence establishment, *S. cerevisiae* cells assemble a
76 bundle composed of stable parallel MTs, hereafter referred to as the Q-nMT bundle, for
77 Quiescent-cell nuclear Microtubule bundle. This structure originates from the nuclear side of
78 the spindle pole body (SPB), the yeast equivalent of the centrosome. It spans the entire
79 nucleus and relocalizes kinetochores and centromeres, which remain attached to MT +ends
80 (Laporte and Sagot, 2014; Laporte et al., 2013). Because the MTs embedded in the Q-nMT
81 bundle are not all of the same length, the structure has a typical arrow shape. When cells exit

82 quiescence, the Q-nMT bundle depolymerizes and, by pulling the attached centromeres back
83 to the SPB, allows the recovery of the typical Rabl-like configuration of chromosomes found
84 in G1 yeast cells (Jin et al., 1998). The molecular mechanisms underlying the formation of this
85 peculiar stable MT structure and its physiological function(s) are not understood. However,
86 cells defective in Q-nMT bundle formation have a compromised survival in quiescence and a
87 drastically reduced fitness upon cell cycle re-entry (Laporte and Sagot, 2014; Laporte et al.,
88 2013, 2015).

89 Here, we show that Q-nMT bundle formation is a multistep process that follows a
90 precise temporal sequence. The first step relies on AuroraB/Ipl1 activity and requires the
91 kinesin-14 Kar3, its regulator Cik1, and the EB1 homolog Bim1. It leads to the formation of a
92 short (≈ 1 µm) and stable bundle that resembles a half mitotic spindle. Importantly, in this first
93 step, MT polymerization and stabilization are coupled. In a second step, additional MTs
94 polymerize from the SPB, elongate, and are zipped to pre-existing MTs in a Cin8/kinesin-5
95 dependent manner. Complete stabilization of the Q-nMT bundle is achieved in a third and
96 final step that requires the kinesin-5 Kip1. Our observations further indicate that Q-nMT
97 bundle assembly requires both MT-kinetochore attachment and inter-kinetochore
98 interactions. Finally, we show that, upon exit from quiescence, the Q-nMT bundle
99 disassembles from its +ends, each MT depolymerizing in coordination with its neighbors, via
100 the action of the depolymerase Kip3, a member of the kinesin-8 family. Importantly we show
101 that the complete disassembly of the Q-nMT bundle is required for cells to re-enter the
102 proliferation cycle. Overall, this study describes the entire life cycle of a MT structure, from
103 the molecular mechanisms involved in its formation and stabilization to its disassembly and
104 further suggests that this atypical quiescent specific structure acts as a regulator, or "control
105 point", for cell cycle resumption upon exit from quiescence.

106 ## Results

107 **The Q-nMT bundle formation is a three-step process.**

108 We have previously shown that the Q-nMT bundle observed in quiescent cells is a
109 stable nuclear structure (Laporte et al., 2013). To investigate whether the stabilization of the
110 Q-nMT bundle was concomitant with its assembly or whether it assembled first as a dynamic
111 structure, and then gets stabilized, we quantified the Q-nMT bundle length (Fig. 1A) and
112 thickness (Fig. 1B) upon quiescence establishment following carbon source exhaustion. We
113 found that the Q-nMT bundle assembly process could be divided into 3 sequential phases. In
114 an initial phase (phase I), MTs elongated from the SPB to reach ≈0.8 µm. The number of these
115 MTs, referred to as phase I-MTs, was approximately the same as in a mitotic spindle (see inset
116 of Fig. 1B and Sup. Fig. 1A). Importantly, phase I-MTs were resistant to nocodazole (Noc), a
117 MT poison that causes dynamic MT depolymerization, indicating that phase I-MT stabilization
118 was concomitant with their polymerization (Fig. 1A-B). In a second phase, beginning ≈10h after
119 glucose exhaustion, additional MTs emerged from the SPB (phase II-MTs) and elongated along
120 phase-I MTs, nearly doubling the thickness of the phase I MT bundle (Fig. 1B and Sup. Fig. 1A).
121 At this stage, the tip of the newly elongated MTs were unstable (Fig. 1A-B). Complete
122 stabilization of the Q-nMT bundle was achieved ≈48h after glucose exhaustion (phase III).
123 Indeed, after this step, a Noc treatment did not affect either the length or the thickness of the
124 Q-nMT bundle (Fig. 1A-B and Sup. Fig. 1B). Plotting Q-nMT bundle width as a function of length
125 for each individual cell, before and after Noc treatment further revealed the 3 successive
126 phases of the Q-nMT bundle formation (Fig. 1C). Of note, Q-nMT bundles were also observed
127 both in diploid cells upon glucose exhaustion (Sup. Fig. 1C) and in haploid cells transferred to
128 water (Sup. Fig. 1D).

129 To confirm the above observations, first, we followed Nuf2-GFP, a protein that localizes
130 to the MT +end. As expected, movies showed that upon Q-nMT bundle formation initiation,
131 Nuf2-GFP signal relocated from the SPB to the distal part of elongating Q-nMT bundles (Sup.
132 Fig. 1E). In phase II, when cells were treated with Noc, the Nuf2-GFP signal followed
133 depolymerizing MTs (Fig. 1D, left panel), testifying for the instability of phase II-MTs. In
134 contrast, the Nuf2-GFP signal remained immobile upon Noc treatment in phase III, as cells
135 have fully stabilized Q-nMT bundles (Fig. 1D, right panel). Second, we measured the γ-tubulin
136 (Tub4) signal at the SPB and found that Tub4 started to accumulate at the SPB at the beginning
137 of phase I to reach a plateau at the end of phase II (Fig. 1E and Sup. Fig. 1F). Interestingly, the
138 amount of Tub4 at the SPB was proportional to the thickness of the Q-nMT bundle (Sup. Fig.
139 1G). Finally, in order to confirm the two waves of MT elongation, we developed a strain
140 expressing mTQZ-Tub1 from the endogenous TUB1 promoter and mRuby-TUB1 under the
141 ADH2 promoter, a promoter that is derepressed after glucose exhaustion, as confirmed by
142 western blot (Sup. Fig. 1H). We observed that mRuby-TUB1 was incorporated into the Q-nMT
143 bundle only after phase I (Fig. 1F and Sup. Fig. 1H), confirming the existence of a second wave
144 of MT elongation during phase II. All the above experiments led us to propose the model
145 shown in Figure 1G.
146
147 **Q-nMT bundle formation is an essential time-regulated process.**
148 Increasing cytoplasmic viscosity has been shown to dampen MT dynamics (Molines et
149 al., 2022). Upon quiescence establishment, yeast cells undergo a transition from a fluid phase
150 to a solid-like phase (Munder et al., 2016; Joyner et al., 2016) and an acidification (Jacquel et
151 al., 2021) which could contribute to the formation of the Q-nMT bundle. Several lines of
152 evidence suggest that these changes in physicochemical properties are not involved in Q-nMT

153 formation. First, 4-day-old quiescent cells can simultaneously display both dynamic
154 cytoplasmic MTs (cMTs) and a stable Q-nMT bundle (Sup. Fig. 1I and (Laporte et al., 2013)).
155 Second, when we mimicked a fluid phase to solid-like transition in proliferating cells by
156 artificially lowering the pH, no stable MTs were observed, whereas F-actin aggregation was
157 induced (Sup. Fig. 1J) as expected (Peters et al., 2013). Third, 2-day-old quiescent cells
158 exhibiting a phase III Q-nMT bundle were able to grow *de novo* dynamic cMTs after a pulse-
159 chase Noc treatment (Sup. Fig. 1K).

160 Importantly, if Q-nMT bundle formation was solely dependent on physicochemical
161 changes, this structure should be able to assemble in late quiescence. By treating cells with
162 Noc upon glucose exhaustion, we were able to prevent the formation of the Q-nMT bundle in
163 early quiescence (Fig. 1H). Strikingly, when the drug was washed out, no Q-nMT bundle
164 assembled, even 144h after Noc removal (Fig. 1H). These cells had entered quiescence
165 because they had assembled actin bodies (Fig. 1H, right panel), another quiescent cell-specific
166 structure (Sagot et al., 2006). This experiment strongly suggests that Q-nMT formation is a
167 process induced by a transient signal emitted upon glucose exhaustion.

168 We have previously shown that mutants unable to assemble Q-nMT bundles have
169 reduced viability in quiescence and a reduced ability to form colonies upon exit from
170 quiescence (Laporte et al., 2013). To establish a direct link between the absence of the Q-nMT
171 bundle and the above phenotypes, we took advantage of our ability to conditionally prevent
172 Q-nMT bundle formation in WT cells using Noc treatment at the onset of glucose exhaustion.
173 As shown in Sup. Fig. 1L, in the absence of the Q-nMT bundle, WT cells lose viability in
174 quiescence and survivors have a reduced ability to generate a progeny upon exit from
175 quiescence. In contrast, a similar Noc treatment of cells that have already assembled a stable
176 Q-nMT bundle (5-day-old cells) did not affect either the viability in quiescence or quiescence

177 exit efficiency, demonstrating that Noc does not have a toxic effect *per se*. Taken together,
178 these experiments confirm our initial findings that the Q-nMT bundle is important for both
179 cell survival during chronological aging and quiescence exit fitness.
180
181 **Steady state tubulin levels and Tub3 isotype are critical for Q-nMT bundle formation.** We
182 then focused on deciphering the molecular mechanisms involved in Q-nMT bundle formation.
183 Yeast cells express two α-tubulin isotypes, Tub1 and Tub3. In proliferating cells, Tub1
184 constitutes the majority (Aiken et al., 2019; Nsamba et al., 2021; Schatz et al., 1986). In 4-day-
185 old cells, the two α-tubulin isotypes were found embedded in the Q-nMT bundle. This was
186 observed using two different pairs of fluorescent proteins in order to avoid any influence of
187 the FP variants, using both widefield and by expansion microscopy (Fig. 2A and Sup. Fig. 2A).
188 Since Tub3 stabilizes MTs *in vitro* (Bode et al., 2003), it may be key for Q-nMT bundle
189 formation. To test this hypothesis, we first analyzed the phenotype of *tub3Δ* cells. In phase II,
190 *tub3Δ* cells displayed short MT bundles that were sensitive to Noc. In phase III, no MT bundles
191 were detected (Fig. 2B and Sup. Fig. 2C). Thus, in this mutant, the MT bundles assembled
192 during phase I were not stable and eventually collapsed. In *tub3Δ* cells, the steady-state
193 amount of α-tubulin is significantly reduced (Sup. Fig. 2B and (Nsamba et al., 2021)). Thus, the
194 amount of α-tubulin, but not Tub3 itself, may be important for Q-nMT bundle formation.
195 Indeed, mutants defective in α- and β-tubulin folding, such as the prefolding complex mutants
196 *pac10Δ*, *gim3Δ* or *yke2Δ,* or in tubulin heterodimer formation, such as *pac2Δ*, or in β-tubulin
197 folding, such as *cin2Δ* or *cin4Δ*, all of which have a reduced amount of tubulin, were unable to
198 assemble a Q-nMT bundle (Sup. Fig. 2D-E).
199 To identify the role of Tub3 *per se*, we took advantage of the "*Tub1-only*" mutant, in
200 which the *TUB3* gene was replaced by the *TUB1* gene at the *TUB3* locus. This mutant expresses

201 only Tub1 and has an α-tubulin level similar to WT (Sup. Fig. 2B and (Nsamba et al., 2021)).
202 We found that "*Tub1-only*" cells have unstable Q-nMT bundles in phase II, and shorter yet
203 stable Q-nMT bundles in phase III (Fig. 2C and Sup. Fig2. C). Moreover, "*Tub1-only*" Q-nMT
204 bundles were thinner than WT Q-nMT bundles (Fig. 2D). Taken together, our data indicate
205 that Tub3 is involved in MT elongation in phase II, since in the absence of this isotype, phase I
206 MT bundles could assemble and MT bundles could get stabilized in phase III, but the second
207 wave of MT nucleation and elongation was impaired as testified by thinner Q-nMT bundles in
208 both phase II and III.
209
210 **Kinetochores are critical for phase I but dispensable for the maintenance of Q-nMT bundles.**
211 Kinetochore components are enriched at the Q-nMT bundle +end ((Laporte et al.,
212 2013) and Sup. Fig. 3A). We therefore tested whether kinetochore-MT attachment might play
213 a role in Q-nMT bundle formation. First, we disrupted kinetochore-MT attachment upon
214 glucose exhaustion using the well-established *ndc80-1* allele (Cheeseman et al., 2006; DeLuca
215 et al., 2018; Wigge et al., 1998). As shown in Fig. 3A, only very short MT structures were
216 detected in *ndc80-1* cells transferred to 37°C at the onset of quiescence entry, even after 4
217 days at non-permissive temperature (for control see Sup. Fig. 3B). Second, we focused on the
218 chromosome passenger complex (CPC: Bir1/Survivin, Sli15/INCENP, Nbl1/Borealin and
219 Ipl1/Aurora B), a complex known to regulate kinetochore-MT attachment dynamics (Cairo and
220 Lacefield, 2020). We found that inactivation of *IPL1* upon entry into quiescence using the
221 thermosensitive allele *ipl1-1* prevented Q-nMT bundle formation (Sup. Fig. 3C). The absence
222 of Q-nMT bundles in cells harboring the NA-PP1 kinase-sensitive allele *ipl1-5as* indicated that
223 the Ipl1 kinase activity was required for this process (Fig. 3B and Sup. Fig. 3D-E for controls).
224 While we could not detect Ipl1 and Nbl1 in quiescent cells, we found that Sli15-GFP and Bir1-

225 GFP localized along the Q-nMT bundle with an enrichment at the Q-nMT bundle +end (Fig.
226 3C). In 4-day-old *bir1Δ* cells, Q-nMT bundle were shorter and not fully stabilized (Fig. 3D). In
227 addition, inactivation of *SLI15* upon glucose exhaustion using the thermosensitive allele *sli15-*
228 *3* drastically impaired Q-nMT bundle formation (Sup. Fig. 3F). Finally, we examined the
229 involvement of Bim1. Bim1 is a MT +end binding protein that plays a role in kinetochore MT-
230 end on attachment (Dudziak et al., 2021; Thomas et al., 2016) and localizes along the entire
231 Q-nMT bundle (Laporte et al., 2013). In fact, we found that the amount of Bim1 correlated
232 with tubulin incorporation during Q-nMT bundle formation (Sup. Fig. 3G). Bim1 deletion alone
233 has no effect on Q-nMT bundle formation even in the presence of Noc ((Laporte et al., 2013)
234 and Fig. 3D). However, *bim1Δ bir1Δ* cells barely assembled MT structures, and these structures
235 were sensitive to Noc (Fig. 3D). This demonstrates that in the absence of Bim1, Bir1 is critical
236 for Q-nMT bundle stabilization in phase I. Of note, we found that the viability of *bim1Δ bir1Δ*
237 cells in quiescence was drastically reduced (Sup. Fig. 3H). Together, these experiments show
238 that kinetochore-MT attachments are critical for the initiation of Q-nMT bundle formation
239 upon entry into quiescence.

240 We then hypothesized that inter-kinetochore interactions could stabilize parallel MTs
241 embedded in the Q-nMT bundle. To test this idea, we analyzed MT organization in s*lk19Δ* cells
242 which are defective in kinetochore clustering (Richmond et al., 2013). In quiescence, Slk19-
243 GFP was enriched at both ends of the Q-nMT bundles (Fig. 3E). s*lk19Δ* cells displayed shorter
244 and thinner MT structures that were sensitive to Noc (Fig. 3F). Since Bim1 has been implicated
245 in kinetochore-kinetochore interaction, we combined s*lk19Δ* with *bim1Δ.* MT structures
246 detected in s*lk19Δ bim1Δ* cells barely reached ≈1 µm and disappeared upon Noc treatment.
247 In addition, in s*lk19Δ bim1Δ* cells, kinetochores localized as a rosette around the SPB (Fig. 3F)
248 and s*lk19Δ bim1Δ* cell viability was severely impaired (Sup. Fig. 3H). This demonstrates that in

249 the absence of Bim1, Slk19 is required for MT bundling and stabilization in phase I. We then
250 focused on monopolin (Mam1, Lrs4, Hrr25 and Csm1), a complex that is known to cross-link
251 kinetochores (Corbett et al., 2010)). These proteins were found to be expressed in quiescent
252 cells (Sup Fig 3I) and when we analyzed the phenotype of *mam1Δ, lrs4Δ* and *csm1Δ* cells in
253 quiescence, most of them displayed short MT structures often arranged in a star-like array
254 (Fig. 3G-H and Sup. Fig. 3J). As for *bir1Δ* and *slk19Δ*, the combination of *bim1Δ* with monopolin
255 deletion worsened MT structure length and stability (Fig. 3H) as well as cell viability in
256 quiescence (Sup. Fig. 3H). Furthermore, cells deleted for *SPO13*, a gene encoding a protein
257 involved in monopolin recruitment to kinetochores (Lee et al., 2004) showed similar
258 phenotypes (Fig. 3G-H and Sup. Fig. 3H). Collectively, these experiments demonstrate that
259 inter-kinetochore interactions are critical for Q-nMT bundle assembly.

260 Finally, we investigated whether kinetochore-MT interactions were required for the
261 stability of the Q-nMT bundle once it is formed. In 5-day-old WT cells, we used a UV-pulsed
262 laser to break the Q-nMT bundle into two pieces. In most cases, the length of both the
263 released fragment and the fragment attached to the SPB remained constant, with the
264 presence of dynamic cMTs after laser ablation testifying for cell viability (Fig. 3I, Sup. Fig. 3K).
265 In contrast, as expected form previous studies (Khodjakov et al., 2004; Zareiesfandabadi and
266 Elting, 2022), in proliferating cells, dynamic anaphase spindles promptly disassembled after
267 the laser-induced breakage (Sup. Fig. 3L). This indicates that once Q-nMT bundles are formed,
268 they do not require MT-kinetochore interaction to be maintained. Accordingly, inactivation of
269 Ndc80 (Sup Fig. 3B) or Ipl1 (Sup. Fig. 3M) in cells that are already in quiescence had no effect
270 on the Q-nMT bundle maintenance. Thus, once formed, Q-nMT stability is established and
271 maintained throughout its length.

272

273 **Each phase of Q-nMT bundle formation requires specific kinesins.**

274 To further dissect the molecular mechanism of Q-nMT bundle formation, we focused
275 on kinesins. Kar3 is a kinesin that, in complex with its regulator Cik1, can generate parallel MT
276 bundles from a MT organizing center (MTOC) both *in vitro* and in proliferating cells (Manning
277 et al., 1999; Mieck et al., 2015; Molodtsov et al., 2016). In quiescence, we found that Kar3-
278 3GFP localized to the SPB, but also as dots along the Q-nMT bundle (Fig. 4A). In 4-day-old
279 *kar3Δ* cells, the majority of the detected MT structures were extremely short compared to WT
280 (Fig. 4B, for control without Noc see Sup Fig. 4A). Similar results were obtained in *cik1Δ* but
281 not in *vik1Δ* cells, which lack the alternative Kar3 regulators (Fig. 4B). Thus, the Kar3/Cik1
282 complex is required for phase I.

283 Cin8 is a kinesin-5 that cross-links MTs (Bodrug et al., 2020; Pandey et al., 2021; Singh
284 et al., 2018), and as such, could play a role in stabilizing Q-nMT bundles. Cin8 was barely
285 detectable in quiescent cells (Sup. Fig. 4B) and *cin8Δ* cells assembled Q-nMT bundles that were
286 thinner than in WT cells (Fig. 4C-E). However, these thinner bundles were stabilized in phase
287 III (Fig. 4C and Sup. Fig. 4C-D). Taken together, these results strongly suggest that Cin8 is
288 required for MT nucleation and/or elongation in phase II but not for stabilization in phase III.

289 Yeast have an additional kinesin-5 called Kip1 (Fridman et al., 2013). In quiescence,
290 most of the Kip1-GFP signal was observed at the Q-nMT bundle +end (Fig. 4F). In *kip1Δ* cells,
291 phase I was slightly delayed. In phase III, while as thick as WT Q-nMT bundles, MT bundles
292 detected in *kip1Δ* cells were not fully stabilized (Fig. 4G-H and Sup. Fig. 4E). These data
293 demonstrate that Kip1 is required for Q-nMT bundle stabilization in phase III. Of note, in phase
294 I and II, Q-nMT bundles were slightly longer in cells deleted for the kinesin-8 Kip3, a MT
295 depolymerase ((Fukuda et al., 2014), Fig. 4 G-H and Sup. Fig. 4G), but have a WT morphology
296 in cells deleted for Kip2, a kinesin that stabilizes cytoplasmic MTs ((Hibbel et al., 2015); Sup.

297 Fig. 4F-G). Taken together our results demonstrate that each phase of Q-nMT bundle assembly
298 involves specific kinesins.
299
300 **SPB duplication/separation requires Q-nMT bundle disassembly.**
301 Finally, we questioned the molecular mechanism of Q-nMT bundle disassembly upon
302 exit from quiescence. We first found that cycloheximide prevented Q-nMT bundle disassembly
303 indicating that this process requires *de novo* protein synthesis (Fig. 5A). Then we measured Q-
304 nMT bundle thickness upon depolymerization, and found that while Q-nMT bundles
305 shortened, they did not become thinner (Fig. 5B). In agreement, Nuf2-GFP clusters found at
306 the Q-nMT bundle +end moved back to the SPB while the Nuf2-GFP clusters localized along
307 the Q-nMT bundle remained immobile until they are reached by the +end-associated clusters
308 (Sup. Fig. 5A). This shows that not all MT +ends started depolymerizing at the same time, and
309 that longer MTs depolymerized first. This finding is consistent with our model in which MTs
310 are cross-linked along the entire length of the Q-nMT bundle.
311 Since Kip3 is the only well-characterized yeast MT depolymerase, we examined Q-nMT
312 bundle disassembly in *kip3Δ* cells and found that it was drastically delayed (Fig. 5C, Sup. Fig.
313 5B), yet the overall depolymerization rate remained unaffected (Sup. Fig. 5B, left panel). In
314 fact, we found that in WT cells, Kip3 needs to be resynthesized upon exit from quiescence
315 (Sup. Fig. 5C). We searched for proteins that might be involved in Q-nMT bundle disassembly
316 together with Kip3. Among the proteins required for mitotic spindle disassembly, we found
317 that inactivation of *CDC14*, *CDC15*, *CDH1*, *DCC1,* and *TOR1* had no effect on Q-nMT bundle
318 disassembly, as did the inactivation of Ipl1 or proteins involved in kinetochore-MT attachment
319 (Sup. Fig. 5D-G). The only additional actor we found was She1, a dynein regulator (Bergman et
320 al., 2012), whose deletion strongly exacerbated the *kip3Δ* phenotype (Fig. 5C, Sup. Fig. 5H).

321 Thus, Q-nMT bundle disassembly does not rely on the canonical mitotic spindle disassembly
322 machinery, but rather specifically requires Kip3 and She1.

323 Importantly, when we followed quiescence exit at the single cell level,
324 depolymerization of the Q-nMT bundle always preceded SPB duplication/separation (Fig. 5A),
325 in both WT and in *kip3Δ* cells (Sup. Fig. 5B, right panel). When we severely impeded Q-nMT
326 bundle disassembly using *kip3Δ she1Δ*, we found that SPB separation was greatly delayed (Fig.
327 5D-F, Sup. Fig. 5I-K). Besides, the growth rate of *kip3Δ she1Δ* cells during proliferation is the
328 same as WT cells (Sup. Fig. 5I), and upon quiescence exit, these mutant cells disassembled
329 actin bodies as fast as WT cells (Sup. Fig. 5K), demonstrating that *kip3Δ she1Δ* cells were not
330 impaired in sensing quiescence exit signals. These observations suggest that upon exit from
331 quiescence, the Q-nMT bundle has to be disassembled prior to SPB duplication/separation.

332 **Discussion**

333 Our results shed light on the precise temporal sequences that generate a Q-nMT
334 bundle upon quiescence establishment in yeast. From bacteria to human stem cells, changes
335 in cell physicochemical properties are known to accompany the establishment of quiescence.
336 Among these modifications, cellular volume reduction increases molecular crowding (Joyner
337 et al., 2016), and pH acidification both increases viscosity and causes changes in
338 macromolecule surface charges (Charruyer and Ghadially, 2018; Jacquel et al., 2021; Munder
339 et al., 2016; Persson et al., 2020). Much evidence suggests that these modifications act as
340 triggers for the auto-assembly of several types of enzyme-containing granules (Munder et al.,
341 2016; Petrovska et al., 2014; Rabouille and Alberti, 2017), or complex structures such as P-
342 bodies and Proteasome Storage Granules (Peters et al., 2013; Jacquel et al., 2021; Currie et
343 al., 2023). Recently, Molines and colleagues demonstrated that cytoplasmic viscosity
344 modulates MT dynamics *in vivo* (Molines et al., 2022). Here, we showed that the formation of
345 the Q-nMT bundle does not depend on changes in the physicochemical properties that cells
346 experience at the onset of quiescence establishment (Sup. Fig. 1). In fact, dynamic cMTs and
347 a stable Q-nMT bundle can be observed simultaneously in a quiescent cell (Sup. Fig. 1I), while
348 physicochemical properties evolve in parallel in both the nucleus and the cytoplasm (Joyner
349 et al., 2016). Importantly, cellular volume reduction, pH acidification and increased viscosity
350 are observed within minutes upon glucose starvation (Joyner et al., 2016) whereas the Q-nMT
351 bundles require a couple of days to be fully assembled (Fig. 1). Furthermore, Q-nMT bundle
352 formation cannot be delayed in time (Fig. 1H), and thus likely depends on a transient signal
353 emitted upon glucose depletion. We speculate that the SPB may act as a platform that
354 integrates this signal, and transfers it to the MT machinery in order to assemble a stable MT
355 structure.

356 As it is required for the onset of Q-nMT bundle formation (Fig. 3B), the CPC component
357 Aurora B/Ilp1, a kinase that plays a key role at the MT-kinetochore interface in response to
358 the tension status, could be one of the targets of the aforementioned nutritional signal. In
359 parallel, upon quiescence establishment, chromosome hyper-condensation (Guidi et al., 2015;
360 Rutledge et al., 2015) could modify the tension at the kinetochore/MT interface and, as such,
361 could contribute to the initiation of phase I (Fig. 6b). Besides, Bim1 has also been implicated
362 in MT-kinetochore attachment (Dudziak et al., 2021; Akhmanova and Steinmetz, 2015).
363 Although its deletion alone has no effect on Q-nMT bundle formation, its role becomes critical
364 for phase I when kinetochore-MT interactions are already destabilized by the absence of other
365 CPC components, other than Ipl1, such as Bir1 (Fig. 3D). Taken together, these observations
366 suggest that kinetochore-MT interactions are essential for phase I initiation, as confirmed by
367 the absence of Q-nMT bundle in the *ndc80-1* mutant (Fig. 3A).

368 In phase I, SPB-anchored MTs elongate and are concomitantly stabilized (Fig. 1 A-C).
369 This step requires the kinesin-14 Kar3 and its regulator Cik1 (Fig. 4B). During mating
370 (Molodtsov et al., 2016), and in early mitosis, when half-spindles form (Kornakov et al., 2020),
371 Kar3/Cik1, together with Bim1, align and cross-link growing MTs along existing MTs, thereby
372 promoting the organization of MTs into parallel bundles. In mitosis however, the kinesin-
373 14/EB1 complex promotes MT dynamics (Kornakov et al., 2020). It remains to be determined
374 whether the robust MT stabilization in phase I depends on the modification of the kinesin-
375 14/EB1 complex properties and/or on additional specific cross-linker(s) (Fig. 6c).

376 In quiescence, deletion of either Monopolin or *SLK19* results in the formation of short,
377 shattered and flared MT structures, phenotypes that are exacerbated by the deletion of *BIM1*
378 (Fig. 3F-H). Since Monopolin and Slk19 are involved in kinetochore clustering (Plowman et al.,
379 2019; Rabitsch et al., 2003; Tóth et al., 2000; Lee et al., 2004; Mittal et al., 2019; Movshovich

380 et al., 2008; Richmond et al., 2013; Zeng et al., 1999), we speculate that kinetochore-
381 kinetochore interaction may not only help prevent depolymerization of individual MTs, but
382 also constrain elongating phase I MTs and facilitate their concomitant cross-linking (Fig. 6d).

383 With the initiation of phase I, Tub4 begins to accumulate at the SPB to enable the
384 second wave of MT nucleation observed in phase II. As phase II MTs elongate, they are
385 simultaneously stabilized along pre-existing phase I MTs (Fig. 6d). This step relies on the
386 kinesin-5/Cin8 as Q-nMT bundles assembled in *cin8Δ* cells are thinner than WT Q-nMT bundles
387 (Fig. 4C-E). Intriguingly, *in vitro,* the monomeric form of the vertebrate kinesin-5, Eg5,
388 promotes MT nucleation and stabilizes lateral tubulin-tubulin contacts (Chen et al 2019). We
389 assume that in the absence of Cin8, either nucleation of phase II MTs cannot occur, or phase
390 II MTs can elongate, but cannot be cross-linked and stabilized to a pre-existing phase I MT(s)
391 as they grow, and thus rapidly depolymerize. Absence of bundle thickening in phase II is also
392 observed in the "*Tub1-only*" mutant *i.e.* in the absence of Tub3. Tubulin isotypes or tubulin
393 PTMs are known to promote the recruitment of specific kinesins and thereby modify MT
394 properties, see for example (Sirajuddin et al., 2014; Peris et al., 2009; Dunn et al., 2008). Could
395 Tub3 be important for Cin8 recruitment or function during phase II?

396 Following phase II, MTs elongate, but their distal parts (>1 µm) are not yet stable (Fig.
397 1A). Stabilization of full-length Q-nMT bundles is achieved approximately 4 days after glucose
398 exhaustion. This step depends on the kinesin-5/Kip1 (Fig. 4G-H and Sup. Fig. 4E) which is
399 essential for cross-linking and stabilizing elongating MTs during phase III (Fig. 6e). Accordingly,
400 we observed a Kip1 enrichment at the Q-nMT bundle +ends (Fig. 4F). Thus, consistent with
401 their ability to form homo-tetramers capable of cross-linking (Acar et al., 2013; Kapitein et al.,
402 2005; Scholey et al., 2014; Weinger et al., 2011) and stabilizing parallel MTs (Kapitein et al.,
403 2005; Shimamoto et al., 2015; Yukawa et al., 2020) in addition to their role of sliding anti-

404 parallel MTs, the two yeast kinesins 5 are essential for Q-nMT bundle formation. However, in
405 quiescence, as well as in mitosis, Kip1 and Cin8 have non-equivalent functions (Roostalu et al.,
406 2011; Shapira and Gheber, 2016).

407 Thus far, our results indicate that the mechanism of Q-nMT bundle formation is distinct
408 from that of mitotic spindle assembly. Similarly, we show that Q-nMT bundle disassembly does
409 not involve the same pathway as mitotic spindle disassembly as it involves Kip3 (Fig. 5C) but
410 is independent of the anaphase-promoting complex and Aurora B/Ipl1 (Sup. Fig. 5D-G).
411 Interestingly, the longest MTs begin to depolymerize from their +ends first. Then, when they
412 reach the +ends of shorter MTs, the shorter ones proceed to depolymerize alongside them
413 (Sup. Fig. 5A). This cooperative behavior has been observed *in vitro* within parallel MT bundles
414 (Laan et al., 2008). Our data demonstrate that such a comportment does exist *in vivo*.

415 Finally, our data indicate that the Q-nMT bundle is required for the survival of WT cells
416 in quiescence. While we do not yet know why this structure is important for chronological
417 aging, it is clear that the presence of the Q-nMT bundle modifies the organization of the
418 nucleus (Laporte et al., 2013; Laporte and Sagot, 2014; Laporte et al., 2016). Since chromatin
419 organization influences gene expression, one hypothesis could be that the presence of the Q-
420 nMT bundle is required for the expression of genes necessary for cell survival in quiescence.
421 Another attractive hypothesis is that the Q-nMT bundle could be the yeast analog of the
422 mammalian primary cilium. Indeed, these two structures are formed upon proliferation
423 cessation, they are both composed of highly stable parallel MTs, their formation involves MT
424 motors, and they are both templated from the centriole/SPB. More importantly, we show here
425 that Q-nMT disassembly is required to allow SPB separation upon exit from quiescence (Fig.
426 5). Thus, the Q-nMT bundle disassembly may control reentry into the proliferation cycle, just

427 as the primary cilium does in ciliated mammalian cells (Goto et al., 2017; Kim and Tsiokas,

428 2011).

429 ## Materiel and Methods

430 **Yeast strains, plasmids and growth conditions**

431 All the strains used in this study are isogenic to BY4741 (*mat a, leu2Δ0, his3Δ0, ura3Δ0,*
432 *met15Δ0)* or BY4742 (*mat alpha, leu2Δ0, his3Δ0, ura3Δ0, lys2Δ0),* available from GE
433 Healthcare Dharmacon Inc. (UK), except for Fig. 2, in which strains of the S288c background
434 were used (Nsamba et al., 2021) and Sup. Fig. 1F in which the W303 background was used. BY
435 strains carrying GFP fusions were obtained from ThermoFisher Scientific (Waltham, MA, USA).
436 Integrative plasmids p*Tub1-mTurquoise2-Tub1*, p*Tub1-wasabi-Tub1*, p*Tub1-mRUBY2-Tub1*,
437 p*Tub1-mEOS2-Tub1* were a generous gift of Wei-Lih Lee (Markus et al., 2015). The strain
438 expressing SPC42-mRFP1 is a generous gift from E. O'Shea (Huh et al., 2003). The strain
439 expressing TUB4-mTQZ is a generous gift of S. Jaspersen (Burns et al., 2015). The *Ipl1-5as* is a
440 generous gift from A. Marston. *Ipl1-1, ndc80-1* and *Sli15-3* are a generous gift from C. Boone.
441 Three copies of eGFP in tandem were integrated at the 3' end of *DAD2*, *TUB3* or *KAR3*
442 endogenous loci respectively. Plasmids for expressing Nup2-RFP (p3695) or Bim1-3xGFP
443 (p4587) from the endogenous locus were described in (Laporte et al., 2013).

444 For Fig. 1F, *pHIS3:mTurquoise2-Tub1+3'UTR::LEU2* was integrated at the *TUB1* locus,
445 then a pRS303-*ADH2p-mRuby2-Tub1* was integrated at the *HIS3* locus. To generate this
446 plasmid, the *ADH2* promoter was amplified from yeast genomic DNA flanked with NotI and
447 SpeI restrictions sites and inserted in pRS303. The mRuby2-Tub1+3'UTR, including the 116-
448 nucleotide intron and 618 nucleotides downstream of the stop codon was cloned between
449 SpeI/SalI sites.

450 Yeast cells were grown in liquid YPDA medium at 30 °C in flasks as described previously
451 in (Sagot et al., 2006) except for experiments using thermosensitive strains, where cells were
452 first grown at 25 °C then shifted at 37 °C for the indicated time before imaging.

453 The experiment in Sup. Fig. 1J was performed as described in (Orij et al., 2009; Peters
454 et al., 2013). In brief, proliferating cells were transferred at an OD_{600nm} of 0.5 in Hepes buffer
455 (25 mM Hepes, pH 7.4, 200 mM KCl, 1 mM $CaCl_2$, and 2 % dextrose), buffered either at pH 4
456 or 7.5, in the presence of 100 µM CCCP (Sigma-Aldrich). After 150 min 30 °C shaking, cells were
457 imaged (for mTQZ-Tub1) or fixed and stained using Alexa Fluor 568–phalloidin (Invitrogen) as
458 described (Sagot et al., 2006).

459 For live cell imaging, 2 µL of the cell culture were spotted onto a glass slide and
460 immediately imaged at room temperature.

461 For quiescence exit, cells were first incubated 2-3 min in liquid YPD and then 2 µL were
462 spread onto a 2 % agarose microscope pad containing YPD. Individual cells were imaged every
463 hour, up to 6 or 12 h at 21°C. For quiescence exit in presence of cycloheximide (Fig. 5A), cells
464 were pre-incubated 30 min in the presence of the drug prior to quiescence exit. Cycloheximide
465 was used at 180 µM (Sigma-Aldrich), Nocodazole was used at 30 µg/mL (7.5 µM) (Sigma-
466 Aldrich), NA-PP1 was used at 50µM (Sigma-Aldrich).

467 **Fluorescence Microscopy**

468 Cells were observed on a fully-automated Zeiss 200M inverted microscope (Carl Zeiss,
469 Thornwood, NY, USA) equipped with an MS-2000 stage (Applied Scientific Instrumentation,
470 Eugene, OR, USA), a Lambda LS 300 Watt xenon light source (Sutter, Novato, CA, USA), a 100X
471 1.4NA Plan-Apochromat objective, and a 5 position filter turret. For RFP and mRuby2 imaging
472 we used a Cy3 filter (Ex: HQ535/50 nm – Em: HQ610/75 nm – BS: Q565 nm lp). For GFP
473 imaging, we used a FITC filter (excitation, HQ487/25 nm; emission, HQ535/40 nm; beam
474 splitter, Q505 nm lp). For mTurquoise2 imaging we used a DAPI filter (Ex: 360/40 nm – Em:
475 460/50 nm– BS: 400 nm). All the filters are from Chroma Technology Corp. Images were
476 acquired using a CoolSnap HQ camera (Roper Scientific, Tucson, AZ, USA). The microscope,

477 camera, and shutters (Uniblitz, Rochester, NY, USA) were controlled by SlideBook software
478 5.0. (Intelligent Imaging Innovations, Denver, CO, USA).

479 For PALM (Fig. 4E) a Nikon Ti-Eclipse equipped with iLas2 TIRF arm, laser diodes (405,
480 488, 532, 561, 642 nm), a 100x 1.49 oil (TIRF) objective connected to a EMCCD Camera
481 Photometrics Evolve was used.

482 Immunofluorescence was done as in (Laporte et al., 2016) and actin AlexaFluor
483 Phalloidin (Invitrogen) staining as in (Sagot et al., 2006).

484 For expansion microscopy (Sup Fig. 2A and 3A), spheroplasts were obtained as
485 described in (Laporte et al., 2016). After washing in 10 mg/mL NaBH4 in PEMS for 10 min,
486 spheroplasts were seeded on 12 mm round poly-L-lysine coated coverslips, washed twice for
487 30 min in 100 µL PEM-BAL (PEM + 1% BSA) and incubated with the primary antibodies (anti-
488 GFP from mouse; Roche, ref. 11814460001, 1/50; anti-alpha-tubulin from rat; YOL1/34,
489 Abcam, ref. Ab6161, 1/100) for 1 hour at 37°C. Cells were then washed three times in PEM-
490 BAL and incubated with the secondary antibodies (Goat anti-mouse AlexaFluor®488 1/200 and
491 Donkey anti-rat AlexaFluor®555; A11029 and A21434 respectively, ThermoFisher Scientific,
492 Waltham, MA) for 45 min at 37 °C. Cells were then washed three times with PBS. Cells were
493 processed for Expansion Microscopy as previously described in (Bahri et al., 2021).
494 Spheroplasts were incubated for 10 min in 0.25 % GA in PBS, washed in PBS three times for 5
495 min, and processed for gelation. A drop of 100 µL of ExM MS (8.625% (wt/wt) SA, 2.5% (wt/wt)
496 AA, 0.15 % (wt/wt) BIS, 2 M NaCl in 1× PBS) was placed on the chilled parafilm, and coverslips
497 were put on the drop with cells facing the solution and incubated for 3 min. Then the
498 coverslips were transferred to 35 µL of ExM MS supplemented with 0.2 % APS and 0.2 %
499 TEMED, with the initiator (APS) added last. Gelation proceeded for 3 min on ice, and samples
500 were incubated at 37 °C in a humidified chamber in the dark for 1 h. Then coverslips with

501 attached gels were transferred into a six-well plate for incubation in 2 mL of digestion buffer
502 (1× TAE buffer, 0.5% Triton X-100, 0.8 M guanidine hydrochloride, pH ~8.3) supplemented
503 with DAPI (1 µg/mL) for 10-15 min at 37 °C, until the gels detached. Fresh proteinase K at 8
504 units/mL was then added and samples incubated at 37 °C for 30 min. Finally, gels were
505 removed and placed in 10mL petri dishes filled with ddH2O for expansion. Water was
506 exchanged at least twice every 30 min, and incubated in ddH2O overnight at RT. Gels
507 expanded between 4× and 4.2× according to SA purity. Expanded cells were imaged with a
508 UPlanS Apo 100×/1.4 oil immersion objective in an Olympus IX81 microscope (Olympus,
509 Tokyo, Japan). For structured illumination microscopy (Sup Fig. 3A), a ZEISS Elyra 7 Lattice SIM
510 was used.

511 Laser ablation (Fig. 3I and Sup. Fig. 3K-L) was performed at room temperature with a
512 100X oil Plan-Apochromat objective lens (NA 1.4) and an Axio-Observed.Z1 microscope (Carl
513 Zeiss) equipped with a spinning disk confocal (Yokogawa), an EMCCD Evolve camera
514 (Photometrics and Roper Scientific) and 491 nm (100 mW; Cobolt calypso) and 561 nm (100
515 mW; Cobolt Jive) lasers. Images were acquired with Metamorph software (Roper Scientific).
516 Every 30 to 120 s, a Z-series of 0.4 µm steps were acquired. A 355 nm microchip laser (Teem
517 Photonics) with a 21 kHz repetition rate, 0.8 µJ energy/pulse, 2 kW of peak power and 400 ps
518 pulse width, powered with an iLas2 PULSE system (Roper Scientific) was used between 10 to
519 40 % power with one pulse of a spot length of 100 points. Breakage was considered as
520 successful if a non-alignment between the two remaining Q-n MT bundle fragments was
521 observed.

522 In Fig.1H, F; Fig. 2B-C; Fig.3C; Fig. 4D, G; Sup. Fig. 1I; Sup. Fig. 2E and Sup. Fig. 3A, a faint
523 and fuzzy fluorescence signal was detected in some cell cytoplasm using the GFP filter set. This
524 signal is not GFP but rather due to a non-specific yellow background fluorescence.

525 Z-stacks were deconvolved using the Deconvolution Lab plugin (Fig. 1D, F; Fig. 3 C, E-F
526 Fig. 4A, F; Sup. Fig. 1E; Sup. Fig. 2A and Sup. Fig. 4B).
527
528 **Image analysis**
529 Distribution and associated statistics were performed using GraphPad Prism 5
530 (GraphPad Software, Inc. La Jolla, USA) and Excel (Microsoft). Unless specified, a student test
531 (t-test with two independent samples) was used to compare two conditions. Among p-values
532 obtained from biological repetitions in a same experiment (Fig.1A; Fig. 2 B-C; Fig. 3D, F, H; Fig.
533 4 C, H, and Fig. 5C), the indicated p-values are the highest measured among repeated
534 experiments. P-values above 0.05 are indicated, while values below are depicted with **
535 ($0.05>p\text{-value}>1.10^{-4}$) and *** if p-value is less than 1.10^{-5} Histograms and scatter dot plots
536 show the mean and the error bars indicate SD. MT length was measured on MAX-projected
537 images using image-J.
538 For MT fluorescence intensity measurements (Fig. 1B, Fig. 2D and Fig. 4D) a line scan
539 (i1) of 4 pixels width containing both FP signal and background was drawn along MTs on SUM
540 projection images (4 z-plans) using ImageJ. A line of 8 pixels width (at the same location) was
541 drawn in order to calculate the intensity of the surrounding background (i2). The real intensity
542 (ir) was calculated as follow: $int = [i1 - ([(i2 \times i2_{surface}) - (i1 \times i1_{surface})] / (i2_{surface} - i1_{surface})) *$
543 $i1_{surface}]$. We arbitrarily set the 'zero' at 0,5µm before the fluorescence increased onset on the
544 SPB side in order to align all intensity measurements.
545 A similar approach was conducted to measure Tub4 fluorescence intensity (Fig. 1E,
546 Sup. Fig. 1F) *i.e.* (i1) and (i2) were two boxes, the second including the first one. Intensity was
547 calculated as follow: $int = [i1 - ([(i2 \times i2_{surface}) - (i1 \times i1_{surface})] / (i2_{surface} - i1_{surface})) * i1_{surface}]$.

548 For morphometric Q-nMT bundle property distribution (Fig. 1C and 4B) the mean
549 fluorescence intensity was measured in each individual cell, in a finite area localized adjacent
550 to the SPB (0,4 µm – 3-4 Z stack sum projected) as an estimate of Q-nMT bundle width and
551 plotted as a function of the according measured bundle length.

552 For Nuf2-GFP fluorescence intensity measurement at the SPB (Sup. Fig. 1E, bottom
553 panel), GFP and RFP line scan measurements were done on a 4 Z-planes sum projection. The
554 "SPB localization zone" was defined as the length ending 250 µm after the brightest RFP signal
555 of Spc42-RFP. The remaining Q-nMT bundle zone was defined as the "+end zone". The total
556 Nuf2-GFP signal detected along the Q-nMT bundle was set to 100 % to determine the
557 percentage of the signal measured at the "SPB localization zone" and the "+end zone".

558 Normalized Q-nMT bundle length (Fig. 3C) was done after line scan intensity
559 measurements. mTQZ-Tub1 intensity slopes were first aligned on their inflexion points. To
560 compare Q-nMT bundles with different lengths, we first sorted Q-nMT bundles <1.8 µm. After
561 an artificial isotropic expansion, we fit all MT structures to length order. Then, the
562 corresponding mean intensity of the Q-nMT bundle (mTZQ-Tub1) and GFP signal were
563 calculated.

564 To measure Q-nMT bundle depolymerization (Fig. 5A and Sup. Fig. 5B), individual Q-
565 nMT bundle lengths were measured over time. The first length measurement was set to 100
566 %. A fluorescence drop above or equal to 25 % defines the inflexion point of the slope, and
567 was used to align the length measurements of different Q-nMT.

568 The FWHM (Full Width at Half Maximum, Fig. 5B) was calculated by measuring
569 fluorescence intensity of a line crossing perpendicularly to a Q-nMT bundle at 0.5 µm from the
570 SPB, using a sum projection. After fitting the intensity level with a Gaussian distribution and

571 obtaining the standard deviation (σ) value, FWHM was calculated using the equation
572 $2\sqrt{(2\ln 2)}x\sigma$.

573 **Western blots**

574 Western blots were done as described in (Sagot et al., 2006) using anti-GFP antibodies
575 (Abcam); anti-Tat1 antibodies, a generous gift from J-P. Javerzat; antibody against the budding
576 yeast Act1 or Sac6, generous gifts from B. Goode; and anti-TagRFP (mRuby2) antibodies, a
577 generous gift from M. Rojo.

578 **Phenotypical analysis of cells without Q-nMT bundle**

579 WT strains were grown to glucose exhaustion (OD ~6.5, Fig. 1F) or to 5 d (Sup. Fig. 1L),
580 washed-out with "old YPDA" (YPDA medium in which cells were grown for 4 d and then filtered
581 to remove cells) pulsed with either DMSO alone or DMSO containing Noc (30 µg/mL final
582 concentration) for 24 h. Cells were then washed twice in "old YPDA" before being incubated
583 in the same medium. Dead cell measurement was done using methylene blue staining. The
584 capacity of cells to exit quiescence (Sup. Fig. 1L, right panel) was scored after micro-
585 manipulation of live cells (cells not stained with methylene blue) as described in (Laporte et
586 al., 2011).

587

588 ## Supplemental data

589 **Supplementary Figure 1** further describes the 3 steps of Q-nMT bundle formation. It shows
590 the impact of physicochemical cell properties on MT stabilization and demonstrates that the
591 Q-nMT bundle is required for both cell viability in quiescence and quiescence exit fitness.

592 **Supplementary Figure 2** describes the impact of the alpha tubulin level on Q-nMT bundle
593 assembly.

594 **Supplementary Figure 3** demonstrates that kinetochore-MT interactions are not required for
595 Q-nMT bundle maintenance and that mutants affected for kinetochore-kinetochore
596 interactions have reduced viability in quiescence.

597 **Supplementary Figure 4** further describes the impact of kinesin deletion on Q-nMT bundle
598 morphometric parameters.

599 **Supplementary Figure 5** explores Q-nMT bundle disassembly in mutants involved in mitotic
600 spindle dismantlement.

601

Acknowledgments

The authors would like to thank the Bordeaux Imaging Center for the help in super-resolution imaging. We express our gratitude to E. O'Shea, A. Marston, S. Jaspersen, J-P. Javerzat, Wei-Lih Lee, C. Boone and B. Goode for sharing reagents and M. Rojo for providing us with the mCherry specific antibodies. We thank Michaël Gué (Zeiss) for helping us a with the lattice SIM Elyra 7 microscope. DL, AML, JD and IS were supported by a grant from the ANR-21-CE13-0023-01, La Ligue Contre le Cancer Régionale – Dordogne grant #193366 and the CNRS. MG and EN were supported by a National Science Foundation grant number MCB-1846262. AR was supported by the Conseil Régional d'Aquitaine (#20111301010) and the CNRS.

Author Contributions

D. Laporte did all the experiments described in this manuscript, except Fig. 1F, 1H, Fig. 5 D-F, Sup. 1H, Sup. 3E, J and Sup. Fig. 5I to K that were performed by A. Massoni-Laporte, together with all image deconvolution, and Sup. Fig. 2A and 3A that were done by J. Dompierre. A. Royou helped for pulse-laser experiments of Fig. 3I and Sup Fig. 3K-L. C. Lefranc did molecular cloning and western blots. D. Mauboules performed yeast genetic for Fig. 2. M. L. Gupta Jr and E. T. Nsamba created the Tub1-only mutant (Fig. 2). L. Gal and M. Schuldiner performed high throughput deletion screen that originally uncovered mutants involved in Q-nMT bundle formation. IS and DL designed and supervised the experiments. IS and DL wrote the manuscript.

624 **References**

625 Acar, S., D.B. Carlson, M.S. Budamagunta, V. Yarov-Yarovoy, J.J. Correia, M.R. Niñonuevo, W. Jia, L.
626 Tao, J.A. Leary, J.C. Voss, J.E. Evans, and J.M. Scholey. 2013. The bipolar assembly domain of
627 the mitotic motor kinesin-5. *Nat Commun*. 4:1343. doi:10.1038/ncomms2348.

628 Aiken, J., J.K. Moore, and E.A. Bates. 2019. TUBA1A mutations identified in lissencephaly patients
629 dominantly disrupt neuronal migration and impair dynein activity. *Human Molecular*
630 *Genetics*. 28:1227–1243. doi:10.1093/hmg/ddy416.

631 Akhmanova, A., and M.O. Steinmetz. 2015. Control of microtubule organization and dynamics: two
632 ends in the limelight. *Nature Reviews Molecular Cell Biology*. 16:711–726.
633 doi:10.1038/nrm4084.

634 Anvarian, Z., K. Mykytyn, S. Mukhopadhyay, L.B. Pedersen, and S.T. Christensen. 2019. Cellular
635 signalling by primary cilia in development, organ function and disease. *Nat Rev Nephrol*.
636 15:199–219. doi:10.1038/s41581-019-0116-9.

637 Baas, P.W., A.N. Rao, A.J. Matamoros, and L. Leo. 2016. Stability properties of neuronal microtubules.
638 *Cytoskeleton (Hoboken)*. 73:442–460. doi:10.1002/cm.21286.

639 Bahri, H., J. Buratto, M. Rojo, J.P. Dompierre, B. Salin, C. Blancard, S. Cuvellier, M. Rose, A. Ben
640 Ammar Elgaaied, E. Tetaud, J.-P. di Rago, A. Devin, and S. Duvezin-Caubet. 2021. TMEM70
641 forms oligomeric scaffolds within mitochondrial cristae promoting in situ assembly of
642 mammalian ATP synthase proton channel. *Biochim Biophys Acta Mol Cell Res*. 1868:118942.
643 doi:10.1016/j.bbamcr.2020.118942.

644 Bergman, Z.J., X. Xia, I.A. Amaro, and T.C. Huffaker. 2012. Constitutive dynein activity in She1
645 mutants reveals differences in microtubule attachment at the yeast spindle pole body. *Mol*
646 *Biol Cell*. 23:2319–2326. doi:10.1091/mbc.E12-03-0223.

647 Bodakuntla, S., A.S. Jijumon, C. Villablanca, C. Gonzalez-Billault, and C. Janke. 2019. Microtubule-
648 Associated Proteins: Structuring the Cytoskeleton. *Trends Cell Biol*. 29:804–819.
649 doi:10.1016/j.tcb.2019.07.004.

650 Bode, C.J., M.L. Gupta, K.A. Suprenant, and R.H. Himes. 2003. The two alpha-tubulin isotypes in
651 budding yeast have opposing effects on microtubule dynamics in vitro. *EMBO Rep.* 4:94–99.
652 doi:10.1038/sj.embor.embor716.

653 Bodrug, T., E.M. Wilson-Kubalek, S. Nithianantham, A.F. Thompson, A. Alfieri, I. Gaska, J. Major, G.
654 Debs, S. Inagaki, P. Gutierrez, L. Gheber, R.J. McKenney, C.V. Sindelar, R. Milligan, J. Stumpff,
655 S.S. Rosenfeld, S.T. Forth, and J. Al-Bassam. 2020. The kinesin-5 tail domain directly
656 modulates the mechanochemical cycle of the motor domain for anti-parallel microtubule
657 sliding. *eLife*. 9:e51131. doi:10.7554/eLife.51131.

658 Burns, S., J.S. Avena, J.R. Unruh, Z. Yu, S.E. Smith, B.D. Slaughter, M. Winey, and S.L. Jaspersen. 2015.
659 Structured illumination with particle averaging reveals novel roles for yeast centrosome
660 components during duplication. *Elife*. 4. doi:10.7554/eLife.08586.

661 Cairo, G., and S. Lacefield. 2020. Establishing correct kinetochore-microtubule attachments in mitosis
662 and meiosis. *Essays in Biochemistry*. 64:277–287. doi:10.1042/EBC20190072.

663 Charruyer, A., and R. Ghadially. 2018. Influence of pH on Skin Stem Cells and Their Differentiation.
664 *Curr Probl Dermatol*. 54:71–78. doi:10.1159/000489520.

665 Cheeseman, I.M., J.S. Chappie, E.M. Wilson-Kubalek, and A. Desai. 2006. The conserved KMN
666 network constitutes the core microtubule-binding site of the kinetochore. *Cell*. 127:983–997.
667 doi:10.1016/j.cell.2006.09.039.

668 Cleary, J.M., and W.O. Hancock. 2021. Molecular mechanisms underlying microtubule
669 growth dynamics. *Curr Biol*. 31:R560–R573. doi:10.1016/j.cub.2021.02.035.

670 Corbett, K.D., C.K. Yip, L.-S. Ee, T. Walz, A. Amon, and S.C. Harrison. 2010. The monopolin complex
671 crosslinks kinetochore components to regulate chromosome-microtubule attachments. *Cell*.
672 142:556–567. doi:10.1016/j.cell.2010.07.017.

673 Currie, S.L., W. Xing, D. Muhlrad, C.J. Decker, R. Parker, and M.K. Rosen. 2023. Quantitative
674 reconstitution of yeast RNA processing bodies. *Proc Natl Acad Sci U S A*. 120:e2214064120.
675 doi:10.1073/pnas.2214064120.

676 DeLuca, K.F., A. Meppelink, A.J. Broad, J.E. Mick, O.B. Peersen, S. Pektas, S.M.A. Lens, and J.G.
677 DeLuca. 2018. Aurora A kinase phosphorylates Hec1 to regulate metaphase kinetochore-
678 microtubule dynamics. *J Cell Biol*. 217:163–177. doi:10.1083/jcb.201707160.

679 Dudziak, A., L. Engelhard, C. Bourque, B.U. Klink, P. Rombaut, N. Kornakov, K. Jänen, F. Herzog, C.
680 Gatsogiannis, and S. Westermann. 2021. Phospho-regulated Bim1/EB1 interactions trigger
681 Dam1c ring assembly at the budding yeast outer kinetochore. *EMBO J*. 40:e108004.
682 doi:10.15252/embj.2021108004.

683 Dunn, S., E.E. Morrison, T.B. Liverpool, C. Molina-París, R.A. Cross, M.C. Alonso, and M. Peckham.
684 2008. Differential trafficking of Kif5c on tyrosinated and detyrosinated microtubules in live
685 cells. *J Cell Sci*. 121:1085–1095. doi:10.1242/jcs.026492.

686 Fridman, V., A. Gerson-Gurwitz, O. Shapira, N. Movshovich, S. Lakämper, C.F. Schmidt, and L. Gheber.
687 2013. Kinesin-5 Kip1 is a bi-directional motor that stabilizes microtubules and tracks their
688 plus-ends in vivo. *J Cell Sci*. 126:4147–4159. doi:10.1242/jcs.125153.

689 Fukuda, Y., A. Luchniak, E.R. Murphy, and M.L. Gupta. 2014. Spatial control of microtubule length and
690 lifetime by opposing stabilizing and destabilizing functions of Kinesin-8. *Curr Biol*. 24:1826–
691 1835. doi:10.1016/j.cub.2014.06.069.

692 Goodson, H.V., and E.M. Jonasson. 2018. Microtubules and Microtubule-Associated Proteins. *Cold*
693 *Spring Harb Perspect Biol*. 10:a022608. doi:10.1101/cshperspect.a022608.

694 Goto, H., H. Inaba, and M. Inagaki. 2017. Mechanisms of ciliogenesis suppression in dividing cells. *Cell*
695 *Mol Life Sci*. 74:881–890. doi:10.1007/s00018-016-2369-9.

696 Gudimchuk, N.B., and J.R. McIntosh. 2021. Regulation of microtubule dynamics, mechanics and
697 function through the growing tip. *Nat Rev Mol Cell Biol*. 22:777–795. doi:10.1038/s41580-
698 021-00399-x.

699 Guidi, M., M. Ruault, M. Marbouty, I. Loïodice, A. Cournac, C. Billaudeau, A. Hocher, J. Mozziconacci,
700 R. Koszul, and A. Taddei. 2015. Spatial reorganization of telomeres in long-lived quiescent
701 cells. *Genome Biol.* 16:206. doi:10.1186/s13059-015-0766-2.

Hahn, I., A. Voelzmann, Y.-T. Liew, B. Costa-Gomes, and A. Prokop. 2019. The model of local axon homeostasis - explaining the role and regulation of microtubule bundles in axon maintenance and pathology. *Neural Dev*. 14:11. doi:10.1186/s13064-019-0134-0.

Heald, R., and A. Khodjakov. 2015. Thirty years of search and capture: The complex simplicity of mitotic spindle assembly. *J Cell Biol*. 211:1103–1111. doi:10.1083/jcb.201510015.

Hibbel, A., A. Bogdanova, M. Mahamdeh, A. Jannasch, M. Storch, E. Schäffer, D. Liakopoulos, and J. Howard. 2015. Kinesin Kip2 enhances microtubule growth in vitro through length-dependent feedback on polymerization and catastrophe. *Elife*. 4:e10542. doi:10.7554/eLife.10542.

Huh, W.-K., J.V. Falvo, L.C. Gerke, A.S. Carroll, R.W. Howson, J.S. Weissman, and E.K. O'Shea. 2003. Global analysis of protein localization in budding yeast. *Nature*. 425:686–691. doi:10.1038/nature02026.

Jacquel, B., T. Aspert, D. Laporte, I. Sagot, and G. Charvin. 2021. Monitoring single-cell dynamics of entry into quiescence during an unperturbed life cycle. *Elife*. 10:e73186. doi:10.7554/eLife.73186.

Janke, C., and M.M. Magiera. 2020. The tubulin code and its role in controlling microtubule properties and functions. *Nat Rev Mol Cell Biol*. 21:307–326. doi:10.1038/s41580-020-0214-3.

Jin, Q., E. Trelles-Sticken, H. Scherthan, and J. Loidl. 1998. Yeast nuclei display prominent centromere clustering that is reduced in nondividing cells and in meiotic prophase. *J. Cell Biol.* 141:21–29.

Joyner, R.P., J.H. Tang, J. Helenius, E. Dultz, C. Brune, L.J. Holt, S. Huet, D.J. Müller, and K. Weis. 2016. A glucose-starvation response regulates the diffusion of macromolecules. *Elife*. 5. doi:10.7554/eLife.09376.

Kapitein, L.C., E.J.G. Peterman, B.H. Kwok, J.H. Kim, T.M. Kapoor, and C.F. Schmidt. 2005. The bipolar mitotic kinesin Eg5 moves on both microtubules that it crosslinks. *Nature*. 435:114–118. doi:10.1038/nature03503.

Khodjakov, A., S. La Terra, and F. Chang. 2004. Laser Microsurgery in Fission Yeast: Role of the Mitotic Spindle Midzone in Anaphase B. *Current Biology*. 14:1330–1340. doi:10.1016/j.cub.2004.07.028.

Kim, S., and L. Tsiokas. 2011. Cilia and cell cycle re-entry: more than a coincidence. *Cell Cycle*. 10:2683–2690. doi:10.4161/cc.10.16.17009.

Kirschner, M., and T. Mitchison. 1986. Beyond self-assembly: from microtubules to morphogenesis. *Cell*. 45:329–342.

Kornakov, N., B. Möllers, and S. Westermann. 2020. The EB1-Kinesin-14 complex is required for efficient metaphase spindle assembly and kinetochore bi-orientation. *J Cell Biol*. 219. doi:10.1083/jcb.202003072.

Laan, L., J. Husson, E.L. Munteanu, J.W.J. Kerssemakers, and M. Dogterom. 2008. Force-generation and dynamic instability of microtubule bundles. *Proc Natl Acad Sci U S A*. 105:8920–8925. doi:10.1073/pnas.0710311105.

740 Laporte, D., F. Courtout, B. Pinson, J. Dompierre, B. Salin, L. Brocard, and I. Sagot. 2015. A stable
741 microtubule array drives fission yeast polarity reestablishment upon quiescence exit. *J. Cell*
742 *Biol.* 210:99–113. doi:10.1083/jcb.201502025.

743 Laporte, D., F. Courtout, B. Salin, J. Ceschin, and I. Sagot. 2013. An array of nuclear microtubules
744 reorganizes the budding yeast nucleus during quiescence. *J. Cell Biol.* 203:585–594.
745 doi:10.1083/jcb.201306075.

746 Laporte, D., F. Courtout, S. Tollis, and I. Sagot. 2016. Quiescent Saccharomyces cerevisiae forms
747 telomere hyperclusters at the nuclear membrane vicinity through a multifaceted mechanism
748 involving Esc1, the Sir complex, and chromatin condensation. *Mol. Biol. Cell*. 27:1875–1884.
749 doi:10.1091/mbc.E16-01-0069.

750 Laporte, D., and I. Sagot. 2014. Microtubules move the nucleus to quiescence. *Nucleus*. 5:113–118.
751 doi:10.4161/nucl.28538.

752 Lee, B.H., B.M. Kiburz, and A. Amon. 2004. Spo13 maintains centromeric cohesion and kinetochore
753 coorientation during meiosis I. *Curr Biol*. 14:2168–2182. doi:10.1016/j.cub.2004.12.033.

754 Liu, P., M. Würtz, E. Zupa, S. Pfeffer, and E. Schiebel. 2021. Microtubule nucleation: The waltz
755 between γ-tubulin ring complex and associated proteins. *Curr Opin Cell Biol*. 68:124–131.
756 doi:10.1016/j.ceb.2020.10.004.

757 Manning, B.D., J.G. Barrett, J.A. Wallace, H. Granok, and M. Snyder. 1999. Differential regulation of
758 the Kar3p kinesin-related protein by two associated proteins, Cik1p and Vik1p. *J Cell Biol*.
759 144:1219–1233. doi:10.1083/jcb.144.6.1219.

760 Markus, S.M., S. Omer, K. Baranowski, and W.-L. Lee. 2015. Improved Plasmids for Fluorescent
761 Protein Tagging of Microtubules in Saccharomyces cerevisiae. *Traffic*. 16:773–786.
762 doi:10.1111/tra.12276.

763 Meiring, J.C.M., B.I. Shneyer, and A. Akhmanova. 2020. Generation and regulation of microtubule
764 network asymmetry to drive cell polarity. *Curr Opin Cell Biol*. 62:86–95.
765 doi:10.1016/j.ceb.2019.10.004.

766 Mieck, C., M.I. Molodtsov, K. Drzewicka, B. van der Vaart, G. Litos, G. Schmauss, A. Vaziri, and S.
767 Westermann. 2015. Non-catalytic motor domains enable processive movement and
768 functional diversification of the kinesin-14 Kar3. *eLife*. 4:e04489. doi:10.7554/eLife.04489.

769 Mitchison, T., and M. Kirschner. 1984. Dynamic instability of microtubule growth. *Nature*. 312:237–
770 242.

771 Mittal, P., A. Chavan, D. Trakroo, S. Shah, and S.K. Ghosh. 2019. Outer kinetochore protein Dam1
772 promotes centromere clustering in parallel with Slk19 in budding yeast. *Chromosoma*.
773 128:133–148. doi:10.1007/s00412-019-00694-9.

774 Molines, A.T., J. Lemière, M. Gazzola, I.E. Steinmark, C.H. Edrington, C.-T. Hsu, P. Real-Calderon, K.
775 Suhling, G. Goshima, L.J. Holt, M. Thery, G.J. Brouhard, and F. Chang. 2022. Physical
776 properties of the cytoplasm modulate the rates of microtubule polymerization and
777 depolymerization. *Developmental Cell*. 57:466-479.e6. doi:10.1016/j.devcel.2022.02.001.

778 Molodtsov, M.I., C. Mieck, J. Dobbelaere, A. Dammermann, S. Westermann, and A. Vaziri. 2016. A
779 Force-Induced Directional Switch of a Molecular Motor Enables Parallel Microtubule Bundle
780 Formation. *Cell*. 167:539-552.e14. doi:10.1016/j.cell.2016.09.029.

781 Movshovich, N., V. Fridman, A. Gerson-Gurwitz, I. Shumacher, I. Gertsberg, A. Fich, M.A. Hoyt, B.
782 Katz, and L. Gheber. 2008. Slk19-dependent mid-anaphase pause in kinesin-5-mutated cells. *J*
783 *Cell Sci*. 121:2529–2539. doi:10.1242/jcs.022996.

784 Munder, M.C., D. Midtvedt, T. Franzmann, E. Nüske, O. Otto, M. Herbig, E. Ulbricht, P. Müller, A.
785 Taubenberger, S. Maharana, L. Malinovska, D. Richter, J. Guck, V. Zaburdaev, and S. Alberti.
786 2016. A pH-driven transition of the cytoplasm from a fluid- to a solid-like state promotes
787 entry into dormancy. *eLife*. 5:e09347. doi:10.7554/eLife.09347.

788 Muroyama, A., and T. Lechler. 2017. Microtubule organization, dynamics and functions in
789 differentiated cells. *Development*. 144:3012–3021. doi:10.1242/dev.153171.

790 Nsamba, E.T., A. Bera, M. Costanzo, C. Boone, and M.L. Gupta Jr. 2021. Tubulin isotypes optimize
791 distinct spindle positioning mechanisms during yeast mitosis. *Journal of Cell Biology*.
792 220:e202010155. doi:10.1083/jcb.202010155.

793 Orij, R., J. Postmus, A. Ter Beek, S. Brul, and G.J. Smits. 2009. In vivo measurement of cytosolic and
794 mitochondrial pH using a pH-sensitive GFP derivative in Saccharomyces cerevisiae reveals a
795 relation between intracellular pH and growth. *Microbiology*. 155:268–278.
796 doi:https://doi.org/10.1099/mic.0.022038-0.

797 Pandey, H., M. Popov, A. Goldstein-Levitin, and L. Gheber. 2021. Mechanisms by Which Kinesin-5
798 Motors Perform Their Multiple Intracellular Functions. *Int J Mol Sci*. 22:6420.
799 doi:10.3390/ijms22126420.

800 Peris, L., M. Wagenbach, L. Lafanechère, J. Brocard, A.T. Moore, F. Kozielski, D. Job, L. Wordeman,
801 and A. Andrieux. 2009. Motor-dependent microtubule disassembly driven by tubulin
802 tyrosination. *J Cell Biol*. 185:1159–1166. doi:10.1083/jcb.200902142.

803 Persson, L.B., V.S. Ambati, and O. Brandman. 2020. Cellular Control of Viscosity Counters Changes in
804 Temperature and Energy Availability. *Cell*. 183:1572-1585.e16.
805 doi:10.1016/j.cell.2020.10.017.

806 Peters, L.Z., R. Hazan, M. Breker, M. Schuldiner, and S. Ben-Aroya. 2013. Formation and dissociation
807 of proteasome storage granules are regulated by cytosolic pH. *J. Cell Biol.* 201:663–671.
808 doi:10.1083/jcb.201211146.

809 Petrovska, I., E. Nüske, M.C. Munder, G. Kulasegaran, L. Malinovska, S. Kroschwald, D. Richter, K.
810 Fahmy, K. Gibson, J.-M. Verbavatz, and S. Alberti. 2014. Filament formation by metabolic
811 enzymes is a specific adaptation to an advanced state of cellular starvation. *Elife*.
812 doi:10.7554/eLife.02409.

813 Plowman, R., N. Singh, E.C. Tromer, A. Payan, E. Duro, C. Spanos, J. Rappsilber, B. Snel, G.J.P.L. Kops,
814 K.D. Corbett, and A.L. Marston. 2019. The molecular basis of monopolin recruitment to the
815 kinetochore. *Chromosoma*. 128:331–354. doi:10.1007/s00412-019-00700-0.

816 Rabitsch, K.P., M. Petronczki, J.P. Javerzat, S. Genier, B. Chwalla, A. Schleiffer, T.U. Tanaka, and K.
817 Nasmyth. 2003. Kinetochore recruitment of two nucleolar proteins is required for homolog
818 segregation in meiosis I. *Dev Cell*. 4:535–548. doi:10.1016/s1534-5807(03)00086-8.

819 Rabouille, C., and S. Alberti. 2017. Cell adaptation upon stress: the emerging role of membrane-less
820 compartments. *Curr Opin Cell Biol*. 47:34–42. doi:10.1016/j.ceb.2017.02.006.

821 Richmond, D., R. Rizkallah, F. Liang, M.M. Hurt, and Y. Wang. 2013. Slk19 clusters kinetochores and
822 facilitates chromosome bipolar attachment. *Mol Biol Cell*. 24:566–577. doi:10.1091/mbc.E12-
823 07-0552.

824 Roll-Mecak, A. 2020. The Tubulin Code in Microtubule Dynamics and Information Encoding. *Dev Cell*.
825 54:7–20. doi:10.1016/j.devcel.2020.06.008.

826 Roostalu, J., C. Hentrich, P. Bieling, I.A. Telley, E. Schiebel, and T. Surrey. 2011. Directional Switching
827 of the Kinesin Cin8 Through Motor Coupling. *Science*. doi:10.1126/science.1199945.

828 Roostalu, J., and T. Surrey. 2017. Microtubule nucleation: beyond the template. *Nat. Rev. Mol. Cell*
829 *Biol.* doi:10.1038/nrm.2017.75.

830 Röper, K. 2020. Microtubules enter centre stage for morphogenesis. *Philos Trans R Soc Lond B Biol*
831 *Sci*. 375:20190557. doi:10.1098/rstb.2019.0557.

832 Rutledge, M.T., M. Russo, J.-M. Belton, J. Dekker, and J.R. Broach. 2015. The yeast genome
833 undergoes significant topological reorganization in quiescence. *Nucleic Acids Res.* 43:8299–
834 8313. doi:10.1093/nar/gkv723.

835 Sagot, I., B. Pinson, B. Salin, and B. Daignan-Fornier. 2006. Actin bodies in yeast quiescent cells: an
836 immediately available actin reserve? *Mol. Biol. Cell*. 17:4645–4655. doi:10.1091/mbc.E06-04-
837 0282.

838 Sanchez, A.D., and J.L. Feldman. 2017. Microtubule-organizing centers: from the centrosome to non-
839 centrosomal sites. *Curr. Opin. Cell Biol.* 44:93–101. doi:10.1016/j.ceb.2016.09.003.

840 Schatz, P.J., F. Solomon, and D. Botstein. 1986. Genetically essential and nonessential alpha-tubulin
841 genes specify functionally interchangeable proteins. *Mol Cell Biol*. 6:3722–3733.
842 doi:10.1128/mcb.6.11.3722-3733.1986.

843 Scholey, J.E., S. Nithianantham, J.M. Scholey, and J. Al-Bassam. 2014. Structural basis for the
844 assembly of the mitotic motor Kinesin-5 into bipolar tetramers. *Elife*. 3:e02217.
845 doi:10.7554/eLife.02217.

846 Shapira, O., and L. Gheber. 2016. Motile properties of the bi-directional kinesin-5 Cin8 are affected
847 by phosphorylation in its motor domain. *Sci Rep*. 6:25597. doi:10.1038/srep25597.

848 Shimamoto, Y., S. Forth, and T.M. Kapoor. 2015. Measuring Pushing and Braking Forces Generated by
849 Ensembles of Kinesin-5 Crosslinking Two Microtubules. *Dev Cell*. 34:669–681.
850 doi:10.1016/j.devcel.2015.08.017.

851 Singh, S.K., H. Pandey, J. Al-Bassam, and L. Gheber. 2018. Bidirectional motility of kinesin-5 motor
852 proteins: structural determinants, cumulative functions and physiological roles. *Cell. Mol. Life*
853 *Sci.* 75:1757–1771. doi:10.1007/s00018-018-2754-7.

854 Sirajuddin, M., L.M. Rice, and R.D. Vale. 2014. Regulation of microtubule motors by tubulin isotypes
855 and post-translational modifications. *Nat Cell Biol*. 16:335–344. doi:10.1038/ncb2920.

856 Thawani, A., and S. Petry. 2021. Molecular insight into how γ-TuRC makes microtubules. *J Cell Sci*.
857 134:jcs245464. doi:10.1242/jcs.245464.

858 Thomas, G.E., K. Bandopadhyay, S. Sutradhar, M.R. Renjith, P. Singh, K.K. Gireesh, S. Simon, B.
859 Badarudeen, H. Gupta, M. Banerjee, R. Paul, J. Mitra, and T.K. Manna. 2016. EB1 regulates
860 attachment of Ska1 with microtubules by forming extended structures on the microtubule
861 lattice. *Nat Commun*. 7:11665. doi:10.1038/ncomms11665.

862 Tóth, A., K.P. Rabitsch, M. Gálová, A. Schleiffer, S.B. Buonomo, and K. Nasmyth. 2000. Functional
863 genomics identifies monopolin: a kinetochore protein required for segregation of homologs
864 during meiosis i. *Cell*. 103:1155–1168. doi:10.1016/s0092-8674(00)00217-8.

865 Weinger, J.S., M. Qiu, G. Yang, and T.M. Kapoor. 2011. A nonmotor microtubule binding site in
866 kinesin-5 is required for filament crosslinking and sliding. *Curr Biol*. 21:154–160.
867 doi:10.1016/j.cub.2010.12.038.

868 Wheway, G., L. Nazlamova, and J.T. Hancock. 2018. Signaling through the Primary Cilium. *Frontiers in*
869 *Cell and Developmental Biology*. 6.

870 Wigge, P.A., O.N. Jensen, S. Holmes, S. Souès, M. Mann, and J.V. Kilmartin. 1998. Analysis of the
871 Saccharomyces spindle pole by matrix-assisted laser desorption/ionization (MALDI) mass
872 spectrometry. *J. Cell Biol.* 141:967–977.

873 Winey, M., and K. Bloom. 2012. Mitotic spindle form and function. *Genetics*. 190:1197–1224.
874 doi:10.1534/genetics.111.128710.

875 Yukawa, M., Y. Teratani, and T. Toda. 2020. How Essential Kinesin-5 Becomes Non-Essential in Fission
876 Yeast: Force Balance and Microtubule Dynamics Matter. *Cells*. 9:E1154.
877 doi:10.3390/cells9051154.

878 Zareiesfandabadi, P., and M.W. Elting. 2022. Force by minus-end motors Dhc1 and Klp2 collapses the
879 S. pombe spindle after laser ablation. *Biophysical Journal*. 121:263–276.
880 doi:10.1016/j.bpj.2021.12.019.

881 Zeng, X., J.A. Kahana, P.A. Silver, M.K. Morphew, J.R. McIntosh, I.T. Fitch, J. Carbon, and W.S.
882 Saunders. 1999. Slk19p is a centromere protein that functions to stabilize mitotic spindles. *J*
883 *Cell Biol*. 146:415–425. doi:10.1083/jcb.146.2.415.

884

885

886 **Abbreviations**

887 MT: microtubule

888 SPB: spindle pole body

889 GTP: guanosine triphosphate

890 MTOC: microtubule organizing center

891 ɣ-TuC: ɣ-tubulin complex

892 MAPs: microtubule associated proteins

893 Q-nMT bundle: quiescence specific nuclear microtubule bundle

894 CPC : chromosome passenger complex

895

896 ## Figure legends

897 **Figure 1: The formation of the Q-nMT bundle is a three-step process.**

898 **(A)** Nuclear MT length in WT cells expressing mTQZ-Tub1, before (**-**) or after (**+**) a 15 min Noc
899 treatment (30 µg/ml) upon entry into quiescence. Each circle corresponds to the length of an
900 individual MT structure. The results for 3 independent experiments are shown (pale blue, cyan
901 and dark blue, n > 160 for each point in each experiment). The mean and SD are shown.
902 Student test or ANOVA (sample >2) were used to compare inter-replicates. #: p-value > 0.05,
903 $: p-value < 0.05. A student test (t-test with two independent samples) was used to compare
904 the results obtained with or without Noc, the indicated p-values being the highest measured
905 among experiments. ***: p-value < 1.10^{-5}. Images of representative cells are shown. Bar is 2
906 µm.

907 **(B)** MT fluorescence intensity as a proxy of MT structure width in WT cells expressing mTQZ-
908 Tub1. Mean intensity measurement for half pre-anaphase mitotic spindles (purple), phase I
909 (green), phase II (orange) or phase III (red) Q-nMT bundle. A line scan along the MT structure
910 for an individual cell is shown as thin line, the mean as a bold line (n > 60 / phase), all the lines
911 being aligned at 0,5 µm before the fluorescence intensity increase onset on the SPB side. The
912 blue lines are results obtained after a 15 min Noc treatment (30 µg/ml). In each graph,
913 horizontal dashed line indicates the mean intensity. Images in pseudo-colors of a
914 representative cell for each phase are shown. Bar is 2 µm.

915 **(C)** MT bundle length as a function of MT bundle width for individual cells in each phase before
916 and after a 15 min Noc treatment (30 µg/ml) in WT cells expressing mTQZ-Tub1. Each circle
917 represents an individual MT structure.

918 **(D)** WT cells expressing mTQZ-Tub1 (red) and Nuf2-GFP (green) in phase II (23 h) or phase III
919 (50 h) were deposited on an agarose pad containing 30 µg/ml Noc and imaged. Blue
920 arrowheads: SPB; white arrowheads: Nuf2-GFP clusters. Time is in min after deposition on the
921 pad. Bar is 1 µm.
922 **(E)** Tub4-mTQZ fluorescence intensity measured at the SPB upon entry into quiescence. Each
923 circle represents an individual cell. The mean and SD are shown; t-tests were used to compare
924 independent samples (N = 3, n > 150), *: 0.05 > p-value > 1.10^{-3}, ***: p-value < 1.10^{-5}. Images
925 in pseudo-colors of representative cells are shown. Bar is 2 µm.
926 **(F)** WT cells expressing mTQZ-Tub1 under the *TUB1* promoter and mRuby-Tub1 under the
927 *ADH2* promoter. The percentage of cells harboring both mTQZ and mRuby fluorescence along
928 the Q-nMT bundle is shown; each circle being the percentage for an independent experiment,
929 with n > 200 counted for each experiment. The mean and SD are shown. Images of
930 representative cells at the indicated time after glucose exhaustion are shown. Bar is 2 µm.
931 **(G)** Schematic of the Q-nMT bundle formation. During phase I, stable MTs (phase I MT - green)
932 elongate from the SPB (grey). During phase II, the amount of Tub4 (cyan) increases at the SPB.
933 In the meantime, new MTs (phase II MT - orange) elongated from the SPB and are stabilized
934 along the phase I MTs, yet their +ends remain dynamic (dashed lines). After phase III, all MTs
935 are stabilized (red). Nuf2 is schematized as dark blue squares.
936 **(H)** Upon glucose exhaustion, WT cells expressing mTQZ-Tub1 (green) and Nuf2-GFP (red)
937 were pulsed treated with 30 µg/ml Noc (blue) or DMSO (grey) for 24 h. Noc or DMSO were
938 then chased using carbon exhausted medium and cells were imaged. Each circle corresponds
939 to MT structure length in an individual cell. The mean and SD are shown (N = 3, n > 100).
940 Images of representative cells 2 d after the chase and representative cells 4 days after the
941 chase are shown. Tubulin (green) was detected by immunofluorescence, actin (red) by

942 phalloidin and DNA (blue) with DAPI. The mean Q-nMT bundle length (±SD) in the population
943 is indicated.
944
945 **Figure 2: Q-nMT bundle formation is influenced by the alpha-tubulin amount and isotype.**
946 **(A)** WT cells (4 d) expressing either Tub3-3GFP (green) and mTQZ-Tub1 (red, top panel) or
947 Tub3-RFP (red) and mWasabi-Tub1 (green, bottom panel). Blue arrowheads point to SPB, bar
948 is 2 µm.
949 **(B)** Nuclear MT length in WT and *tub3Δ* cells expressing mTQZ-Tub1, 36 h (phase II, orange)
950 and 90 h (phase III, red) after glucose exhaustion, treated 15 min (blue) or not (grey) with 30
951 µg/ml Noc. Each circle corresponds to the length of an individual MT structure, mean and SD
952 are shown. ANOVA was used to compare inter-replicates (n > 200, N = 5); #: p-value > 0.05, $:
953 p-value < 0.05. A student test (t-test with two independent samples) was used to compare (**+**)
954 or (**-**) Noc data. The indicated p-values are the highest calculated among the 5 experiments;
955 ***: p-value < 1.10^{-5}. Images of representative cells are shown, bar is 2 µm.
956 **(C)** Nuclear MT length in WT and *Tub1-only* cells expressing mTQZ-Tub1, 36 h (phase II, orange)
957 and 90 h (phase III, red) after glucose exhaustion, treated 15 min or not with 30 µg/ml Noc.
958 Statistical representations are as in (B). Images of representative cells are shown, bar is 2 µm.
959 **(D)** Fluorescence intensity along the Q-nMT bundle in WT (grey) and *Tub1-only* (blue) cells
960 expressing mTQZ-Tub1 grown for 10 h (phase I), 36 h (phase II), and 90 h (phase III). Individual
961 fluorescent intensity is shown as thin line, the mean as a bold line (n > 60 / phase), all the lines
962 being aligned at 0,5 µm before the fluorescence intensity increase onset on the SPB side.
963 Dashed lines indicate the maximal mean fluorescence intensity. Images in pseudo-color of
964 representative cells are shown, bar is 2 µm.
965

966 **Figure 3: Kinetochore-kinetochore interactions are required for Q-nMT bundle formation.**

967 **(A)** Nuclear MT length distribution in WT (grey) and *ndc80-1* (violet) cells expressing mTQZ-
968 Tub1 (green) and Nuf2-GFP (red), transferred to 37 °C upon glucose exhaustion and
969 maintained at 37 °C for the indicated time. Cells were imaged after a 20 min Noc treatment
970 (30 µg/ml). Each circle corresponds to the length of an individual MT structure, mean and SD
971 are shown. A student test (t-test with two independent samples) was used to compare (**+**) or
972 (**-**) Noc samples from the same experiment (n > 250, N = 2). The indicated p-values are the
973 highest p-values calculated among the 2 repeated experiments. ***: p-value < 1.10^{-5}. Images
974 of representative cells incubated 12 h at 37 °C are shown, bar is 2 µm.

975 **(B)** WT (grey) and *ipl1-5as* (pink) cells expressing mTQZ-Tub1 were treated for 60 h with 50
976 µM NA-PP1 after glucose exhaustion, and imaged after a 15 min Noc treatment (30 µg/ml).
977 Same statistical representation as in (A); N = 2, n > 250. Images of representative cells are
978 shown, bar is 2 µm.

979 **(C)** WT cells (2 d) expressing mTQZ-Tub1 (red) and Bir1-GFP or Sli15-GFP (green) were imaged.
980 Graphs show Bir1-GFP or Sli15-GFP fluorescence intensity along normalized Q-nMT bundles
981 (see material and method section, plain and dash lines: mean and SD respectively). Images of
982 representative cells are shown, bar is 2 µm.

983 **(D)** Nuclear MT length distribution in cells of the indicated genotype (4 d) expressing mTQZ-
984 Tub1 treated or not with Noc (30 µg/ml). Same statistical representation as in (A); N = 3, n >
985 200. Images of representative cells are shown, bar is 2 µm.

986 **(E)** WT cells expressing mTQZ-Tub1 (red) and Slk19-GFP (green) 4 h after glucose exhaustion.
987 Blue arrowhead: SPB, bar is 2 µm.

988 **(F)** Nuclear MT length distribution in cells of the indicated genotype (4 d) expressing mTQZ-
989 Tub1 (green) and Nuf2-GFP (red) imaged before or after Noc treatment (30 µg/ml). Same

990 statistical representation as in (A); N = 2, n > 200. Images of representative cells are shown,
991 white arrowheads point to Nuf2-GFP dots, bar is 2 µm.
992 **(G)** Cells of the indicated genotype (4 d) expressing mTQZ-Tub1 (green) and Nup2-RFP (red);
993 bar is 1 µm.
994 **(H)** Nuclear MT length distribution in cells of the indicated genotype (4 d) expressing mTQZ-
995 Tub1 treated or not with Noc (30 µg/ml). Same statistical representation as in (A); N ≥ 2, n >
996 200. Images of representative cells are shown, bar is 2 µm.
997 **(I)** Length variation of nuclear MT bundle fragments after laser ablation (pink dash line) in cells
998 expressing mRuby-TUB1 (red) and Dad2-GFP (green). Time is in min. Images of representative
999 cells are shown, blue arrowhead: SPB, white arrowhead: cMT, bar is 2 µm. Graph indicates the
1000 variation of length in released fragments (n > 120) and histograms show the % of released or
1001 SBP attached fragments that are either stable, or that shorten or grow within a 30 min period
1002 after the laser-induced breakage. Bar is 1 µm
1003
1004 **Figure 4: Each phase of Q-nMT formation requires a specific kinesin.**
1005 **(A)** Images of representative WT cells (2 d) expressing Kar3-3GFP (green) and mTQZ-Tub1 (red)
1006 and corresponding fluorescence intensity along normalized Q-nMT bundles (see material and
1007 method section), bar is 2 µm.
1008 **(B)** Morphometric Q-nMT bundle properties distribution in 4 d WT (grey), *kar3Δ* (red), *vik1Δ*
1009 (blue), and *cik1Δ* cells (green) expressing mTQZ-Tub1 after Noc treatment (30 µg/ml) – see
1010 Sup. Fig. 4A for the control without Noc. Each circle corresponds to an individual Q-nMT
1011 bundle. Black crosses are mean and SD. Images of representative cells are shown, bar is 2 µm.
1012 **(C)** Nuclear MT length distribution in WT and *cin8Δ* cells expressing mTQZ-Tub1 treated (**+**) or
1013 not (**-**) with 15 min Noc (30 µg/ml). Each circle corresponds to the length of an individual MT

1014 structure, mean and SD are shown. A student test (t-test with two independent samples) was
1015 used to compare (**+**) or (**-**) Noc samples from the same experiment (n > 250, N = 2). The
1016 indicated p-values are the highest p-values calculated among the 2 repeated experiments.
1017 ***: p-value < 1.10^{-5}.
1018 **(D)** Fluorescence intensity along Q-nMT bundles in WT and *cin8Δ* cells expressing mTQZ-Tub1
1019 7 h and 24 h after glucose exhaustion. Thin line: intensity from an individual cell; bold line:
1020 mean intensity (n > 60 / phase). Images of representative cells are shown, bar is 2 µm.
1021 **(E)** WT and *cin8Δ* cells expressing mEOS3.2-Tub1 were imaged using PALM. Images in pseudo-
1022 colors of representative cells are shown. Full width at half maximum (FWHM) was measured
1023 at the indicated distance from the SPB. Each line in the bottom graphs corresponds to a single
1024 cell; p-value between WT and *cin8Δ* are indicated (unpaired t-test). Bar is 2 µm.
1025 **(F)** Images of representative WT cells (3 d) expressing Kip1-GFP (green) and mTQZ-Tub1 (red).
1026 Graphs show fluorescence intensity along normalized Q-nMT bundles (plain and dash lines:
1027 mean and SD respectively). Bar is 2 µm, blue arrowhead: SPB.
1028 **(G)** Representative images of WT, *kip1Δ* and *kip3Δ* cells expressing mTQZ-Tub1 treated (**+**) or
1029 not (**-**) with 15 min Noc (30 µg/ml), Bar is 2 µm.
1030 **(H)** Nuclear MT length distribution in WT, *kip1Δ* and *kip3Δ* cells expressing mTQZ-Tub1 treated
1031 (**+**) or not (**-**) 15 min with Noc (30µg/ml). Legend is the same as in (C); n > 250; *: p-value <
1032 1.10^{-3}; ***: p-value < 1.10^{-6}. MT mean length and SD are indicated.
1033
1034 **Figure 5: Q-nMT bundle disassembly always occurs before SPB separation upon quiescence**
1035 **exit.**
1036 **(A)** WT cells expressing Spc42-RFP (red) and Nuf2-GFP (green) (5 d) were re-fed on an YPDA
1037 microscope pad. Individual Q-nMT bundles were measured in cells treated with DMSO (top

1038 panel, Nuf2-GFP, n=33) or with CHX (bottom panel, Stu2-GFP, n=49). Each line corresponds to
1039 an individual cell. In the upper panel, time was set to zero at the onset of MT bundle
1040 depolymerisation. In the lower panel, time was set to zero when cells were deposited on the
1041 agarose pad, bar is 2 µm

1042 **(B)** Q-nMT bundle length (green) and fluorescence intensity at full width half maximum
1043 (FWHM - orange) were measured upon quiescence exit in WT cells (5 d) expressing mTQZ-
1044 Tub1. Representative example of shrinking Q-nMT bundle is shown on the left, bar is 1 µm.

1045 **(C)** Cells of the indicated genotype expressing mTQZ-Tub1 were grown for 4 d, and re-fed. Q-
1046 nMT bundle length was measured at the indicated time points, 15 min after a Noc treatment
1047 (30 µg/ml), to remove all dynamic cMTs. Each circle corresponds to a single cell. MT mean
1048 length and SD are indicated. A student test (t-test with two independent samples) was used
1049 to compare samples from the same experiment (n > 250, N = 4). The indicated p-values are
1050 the highest p-value calculated among the 4 repeated experiments. ***: p-value < 1.10^{-5}. MT
1051 mean length and SD are indicated. Images of representative 4-day-old cells of the indicated
1052 genotype expressing mTQZ-Tub1 before and 60 min after quiescence exit are shown, bar is 2
1053 µm.

1054 **(D)** Representative images of a *kip3Δ* cell expressing Nuf2-GFP upon quiescence exit. Blue and
1055 white arrowheads: SPBs and Q-nMT bundle extremities respectively, bar is 2 µm.

1056 **(E)** Percentage of 6-day-old cells expressing Spc42-mRFP1 with separated SPB as a function of
1057 time upon quiescence exit (n > 200).

1058 **(F)** WT and *kip3Δshe1Δ* cells (6 d) expressing Spc42-mRFP1 (red) and mTQZ-Tub1 (green) were
1059 re-fed on a YPDA microscope pad. Percentage of cells with a single SBP with or without Q-nMT
1060 bundle or with duplicated SPBs were scored (N = 4, n > 200), SD are indicated. Images of

1061 representative cells are shown, bar is 2 µm. Right bottom panel: actin (phalloidin staining, red)
1062 in *kip3Δ she1Δ* cells (6 d) expressing mTQZ-Tub1 (green) before and 1 h after quiescence exit.
1063

1064 **Figure 6: Model for Q-nMT bundle assembly.**

1065 (a) In G1, the nucleus is in a Rabl-like configuration. (b) Upon quiescence establishment,
1066 chromosomes get condensed. MT-kinetochore interaction and Ilp1 are required for the onset
1067 of phase I. (c) Kar3 and its regulator Cik1 are essential to initiate Q-nMT bundle elongation.
1068 Although deletion of *BIM1* has no effect, it becomes critical for phase I if kinetochore-MT
1069 interactions are destabilized by the absence of Chromosome Passenger Complex components.
1070 Kinetochore clustering by the monopolin complex and Slk19 is needed to maintain MT
1071 bundling while phase I MTs elongate. During phase I, Tub4 (ɣ-Tubulin) accumulates at the SPB.
1072 (d) In phase II, a second wave of MT nucleation and elongation occur. Phase II MTs are
1073 concurrently stabilized along pre-existing phase I MTs, in a Cin8-dependent manner. Phase I
1074 and phase II MT +ends (>1 µm) remain dynamic until the full-length Q-nMT bundle
1075 stabilization is reached via the action of Kip1, about 2 days after glucose exhaustion (e).

1076

1077 ## Supplementary Figure legends

1078 **Supplementary Figure 1**

1079 **(A)** Fluorescence intensity along MT structures in WT cells expressing mTQZ-Tub1. Mean
1080 intensity measurement for half pre-anaphase mitotic spindles (violet, n = 60), phase I (green,
1081 n = 19), and phase II (orange, n= 22) Q-nMT bundles. A line scan along the MT structure for an
1082 individual cell is shown as thin line, the mean as a bold line, all the lines being aligned at 0,5
1083 µm before the fluorescence intensity increase onset on the SPB side.

1084 **(B)** Individual Q-nMT bundle full width measured at half-maximum in WT cells (4 d) expressing
1085 mTQZ-Tub1 before or after 1 h after Noc treatment. A paired t-test was use to compare the
1086 two conditions (n > 40).

1087 **(C)** Nuclear MT length in WT haploid (mat a and mat α) or diploid (mat a/mat α) cells
1088 expressing mTQZ- Tub1. Each circle represents an individual cell. Mean and SD are shown in
1089 red.

1090 **(D)** Nuclear MT length in WT proliferating cells expressing mTQZ-Tub1 transferred to water,
1091 treated (**+**) or not (**-**) 15 min with 30 µg/ml Noc. Image of representative cells are shown, bar
1092 is 2 µm.

1093 **(E)** WT cells expressing Spc42-RFP (red) and mTQZ-Tub1 (green, top panel) or Nuf2-GFP
1094 (green, bottom panel) upon entry into quiescence. The percentages indicate the relative
1095 amount of Nuf2-GFP detected at the SBP (blue arrowhead), bar is 1 µm.

1096 **(F)** Tub4-mTQZ fluorescence intensity in WT cells of the W303 background. The mean and SD
1097 are shown; t-test was used to compare independent samples (N = 3, n > 150), ***: p-value <
1098 1.10^{-5}.

1099 **(G)** Fluorescence intensities in WT cells (4 d) expressing Tub4-mTQZ and mRuby-Tub1. The
1100 Tub4-mTQZ signal at the SBP is plotted as a function of the mRuby signal along the Q-nMT
1101 bundle. Each circle represents an individual cell (n = 60).
1102 **(H) Top panel:** western blot using anti-GFP and anti-RFP antibodies on total protein extracts
1103 obtained from the indicated cells upon entry into quiescence. Anti-Ade13 antibodies are used
1104 as loading control. **Bottom panel**: images of representative WT cells expressing only pTUB1-
1105 mTQZ-Tub1 (green) or only pADH2-mRuby-Tub1 (red) upon entry into quiescence as a control
1106 of cross channel fluorescence, bar is 2 µm.
1107 **(I)** WT cells expressing mRuby-Tub1 (4 d) displaying both dynamic cMTs (red arrowhead) and
1108 a Q-nMT bundle (time is in min, bar is 1 µm).
1109 **(J)** An artificial fluid phase to solid-like transition in proliferating cells does not induce MT
1110 stabilization. Proliferating WT cells expressing mTQZ-Tub1 (green) and Spc42-RFP (red) with
1111 fluid (pH = 7.5) or solid-like (pH = 4) cytoplasm/nucleoplasm (see materials and method) were
1112 incubated 15 min with 30 µg/ml Noc (left) or stained with phalloidin to detect actin (right).
1113 Indicated phenotypes were quantified (left and right graphs, N = 2, n > 115, mean and SD are
1114 indicated). Bar is 2 µm.
1115 **(K)** Cells can assemble dynamic cMTs (red arrowhead) in quiescence. 2-day-old WT cells
1116 expressing mRuby-Tub1 were imaged after a 15 min Noc pulse-chase (30 µg/ml, time is in
1117 min). Red arrowhead: cytoplasmic MT, blue arrowhead: SBP, bar is 2 µm.
1118 **(L) Left graphs:** WT cell viability after a 24h-pulse (grey rectangle) with Noc (30 µg/ml, circles)
1119 or DMSO (triangles), followed by a chase using carbon exhausted medium, the Noc pulse being
1120 done either upon glucose exhaustion or 5 days after glucose exhaustion. Each circle/triangle
1121 is the percentage obtained for an independent experiment in which n > 200 cells were scored.
1122 **Right graph:** live cells, as attested by a clear staining after a methylene blue treatment, were

1123 micro-separated 8 days after the Noc pulse done either upon glucose exhaustion or 5 d after
1124 glucose exhaustion, and allowed to give rise to a colony on a YPDA plate. Each circle/triangle
1125 is the percentage obtained for an independent experiment in which n > 100 cells were micro-
1126 separated. Images of representative YPDA plates after 3 d of growth at 30°C are shown. In E
1127 and K, blue arrowhead points to the SBP.

1128 **Supplementary Figure 2**

1129 **(A)** Expansion microscopy images of WT cells (4 d) expressing Tub3-3xGFP and immuno-
1130 stained with GFP (green) and α-tubulin (red) YOL1/2 antibodies, bar is 1 µm.

1131 **(B)** Western blot using α-tubulin YOL1/2 antibody on total protein extracts from the indicated
1132 cells grown for 4 d. Actin was used as a loading reference. Numbers indicate the tubulin/actin
1133 ratio (mean for N = 8).

1134 **(C)** Nuclear MT length in WT, *tub3Δ* and tub1-only cells expressing mTQZ-Tub1, 36 h (phase II,
1135 yellow) and 90 h (phase III, red) after glucose exhaustion, treated 15 min (blue) or not (grey)
1136 with 30 µg/ml Noc. Individual experiments from Fig. 2B and Fig. 2C are shown. P-values for
1137 Anova or unpaired t-test are indicated, ***: p-value < 1.10^{-5}.

1138 **(D)** Nuclear MT length distribution in *yke2Δ*, *pac10Δ* or *gim3Δ* cells (4 d) and in corresponding
1139 WT cells expressing Nuf2-GFP (dark grey bars) or Bim1-3GFP (light grey bars). Right panel:
1140 western blot using an anti-α-tubulin antibody on total protein extracts from cells of the
1141 indicated genotype (4 d). Actin is a loading reference. The tubulin/actin ratio is indicated
1142 (N=4).

1143 **(E)** Nuclear MT length distribution in *pac2Δ*, *cin2Δ* or *cin4Δ* (4 d) and in corresponding WT cells
1144 expressing Bim1-GFP (dark grey bars). Right panel: western blot using an anti-α-tubulin
1145 antibody on total protein extracts from cells of the indicated genotype (4 d). Actin is a loading
1146 reference. The tubulin/actin ratio is indicated (N=4).

1147 **Supplementary Figure 3**

1148 **(A) Upper panel:** WT cell (4 d) expressing Dad2-GFP and immuno-stained with GFP (green)
1149 and α-tubulin (red) YOL1/2 antibodies imaged using expansion microscopy. Blue is DAPI.
1150 **Lower panel:** WT cell (4 d) expressing Dad2-GFP (green) and mRuby-Tub1 (red), imaged using
1151 SIM. Bar is 1 µm.

1152 **(B)** Nuclear MT length distribution in cells of the indicated genotypes, grown for 3 d at 25 °C,
1153 shifted to 37 °C or 25° C for 48 h, and treated 15 min or not with 30 µg/ml Noc. Each circle
1154 corresponds to the length of an individual MT structure, mean and SD are shown. ***: p-value
1155 $< 1.10^{-6}$. Images of representative cells are shown, bar is 2 µm.

1156 **(C)** WT (grey) and *ipl1-1* cells (pink) expressing mTQZ-Tub1 were shifted upon glucose
1157 exhaustion to 37 °C for 48 h, and imaged after a 20 min Noc treatment (30 µg/ml). Same
1158 legend as in (B). Images of representative cells are shown, bar is 2 µm.

1159 **(D)** Nuclear MT length in cells of the indicated genotypes, grown for 60 h in DMSO or 50 µM
1160 NA-PP1, treated 15 min or not with 30 µg/ml Noc. Same legend as in (B). Images of
1161 representative cells are shown, bar is 2 µm.

1162 **(E)** Western blot using anti-myc antibodies on total protein extracts from *ipl1-5as*-myc cells
1163 treated 60 h with DMSO or 50 µM NA-PP1 after quiescence entry. Ade13 is the loading
1164 reference.

1165 **(F)** Nuclear MT length in cells of the indicated genotypes grown 48 h at 37 °C or 96 h at 25 °C,
1166 treated 15 min or not with 30 µg/ml Noc. Same legend as in (B). Images of representative cells
1167 are shown, bar is 2 µm.

1168 **(G)** Distribution of Bim1-3GFP intensity as a function of mTQZ-TUB1 intensity in individual Q-
1169 nMT bundles (green: phase I, 7 h after glucose exhaustion; orange, phase II, 26 h after glucose

1170 exhaustion and red, phase III, 50h after glucose exhaustion). Each circle represents an
1171 individual Q-nMT bundle.

1172 **(H)** Viability (methylene blue staining) after the indicated time in quiescence (left graph), and
1173 capacity to form a colony after single live cell micro-manipulation after 12 days in quiescence
1174 (right graph). Pictures of representative plates 3 d after cell micro-manipulation are shown.

1175 **(I)** Western blot using anti-GFP antibodies on total protein extracts from proliferating or 4-
1176 days-old cells expressing the indicated GFP fusion protein. Ade13 and Act1 are the loading
1177 controls.

1178 **(J)** Percentage of cells of the indicated genotype displaying a MT star-like array. Each circle
1179 represents the % obtained for an independent culture (n > 200). Mean and SD are indicated.

1180 **(K)** WT cells (6 d) expressing mRuby-Tub1 (red) and Nuf2-GFP (green) were transferred onto
1181 an agarose pad. Q-nMT bundles were cut using a pulsed laser (pink dashed line). White
1182 arrowheads point to dynamic cMTs. Time is in min, bar is 2 µm.

1183 **(L)** Proliferating cells expressing mRuby-Tub1 (red) and Dad2-GFP (green) were transferred
1184 onto an agarose pad. Anaphase spindles were cut and the behavior of the released fragments
1185 was followed. Time is in min, bar is 2 µm.

1186 **(M)** Nuclear MT length in cells of the indicated genotypes, grown for 3 d at 25 °C, shifted to
1187 37 °C or 25° C for 48 h, and treated 15 min or not with 30 µg/ml Noc. Same legend as in (B).
1188 Images of representative cells are shown, p-value from unpaired t-test is indicated, bar is 2
1189 µm.

1190

1191 **Supplementary Figure 4**

1192 **(A)** Q-nMT bundle length as a function of Q-nMT bundle width for individual WT cells (grey)
1193 and *kar3Δ* cells (red) 90 h after glucose exhaustion.
1194 **(B)** WT cells expressing mTQZ-Tub1 (red) and Cin8-GFP (green) were imaged at the indicated
1195 times after glucose exhaustion. Cells expressing only mTQZ-Tub1 (left panel) testify for the
1196 absence of fluorescence leak from the mTQZ signal into the GFP channel. Bar is 2µm.
1197 **(C)** Fluorescence intensity along Q-nMT bundles in WT (black) and *cin8Δ* cells expressing
1198 mTQZ-Tub1, treated (green) or not (red) with Noc. Each line is an individual cell, the bold lines
1199 are the mean (n > 20).
1200 **(D)** Morphometric Q-nMT bundle properties distribution in WT (grey) and *cin8Δ* (green) cells
1201 expressing mTQZ-Tub1. Each circle is an individual cell.
1202 **(E)** Fluorescence intensity along Q-nMT bundles in WT (grey, n > 50), *kip1Δ* (red, n > 50), *bim1Δ*
1203 (green, n > 50), and *kip1Δ bim1Δ* (blue, n > 30) cells (4 d). Each line is an individual cell, the
1204 bold lines are the mean.
1205 **(F)** Nuclear MT length distribution in *kip2Δ* cells expressing mTQZ-Tub1, treated 15 min (blue
1206 dots) or not (black dots) with 30 µg/ml Noc. For a comparison, the mean WT length is indicated
1207 as dashed line. Unpaired t-test p-values are indicated.
1208
1209 **Supplementary Figure 5**
1210 **(A)** Representative 5-day-old cells (left and right) expressing mTQZ-Tub1 (red) and Nuf2-GFP
1211 (green) exiting quiescence on a YPDA agarose pad. Blue arrowhead: SBP; white arrows: Nuf2-
1212 GFP cluster. Time is in min, bar is 1µm.
1213 **(B)**. WT and *kip3Δ* cells (5 d) expressing Nuf2-GFP were re-fed on an YPDA microscope pad.
1214 Each line corresponds to an individual cell. Data were presented either (left) with the time set

1215 to zero at the onset MT depolymerisation or (right) at the onset of SPB separation (red dash
1216 line).
1217 **(C)** Western blot using GFP antibodies on total protein extracts from WT cells expressing Kip3-
1218 GFP grown for the indicated time. Sac6 was used as a loading control.

1219 **(D-E)** Nuclear Q-nMT bundle length in cells of the indicated genotype expressing mTQZ-Tub1,
1220 grown for 4 d and imaged at the indicated time after refeeding. For the rapamycin experiment
1221 in (D), WT cells were pre-incubated 1 h with rapamycin (1 µg/mL), and then re-fed in presence
1222 of the drug. For thermo-sensitive strains in (E), cells were grown 4 d at 25 °C, shifted 1 h at 37
1223 °C, and then transferred to new medium at 37 °C to trigger quiescence exit. Measurements
1224 were done after a 15 min Noc treatment (30 µg/ml) to remove dynamic cMTs. Each circle
1225 represents an individual cell. Mean and SD are indicated.
1226 **(F-G)** Nuclear Q-nMT bundle length in cells of the indicated genotype expressing mTQZ-Tub1
1227 were grown for the indicated time at 25 °C, shifted to 37 °C and re-fed. In G, measurements
1228 were done after a 15 min Noc treatment (30 µg/ml) to remove dynamic cMTs. Each circle
1229 represents an individual cell. Mean and SD are indicated.
1230 **(H)** 3 individual experiments in which nuclear MT length was measured in 4-day-old
1231 *kip3Δshe1Δ* cells expressing mTQZ-Tub1 upon quiescence exit (n > 100). P-values from
1232 unpaired t-test are shown. Each circle represents an individual cell. Mean and SD are
1233 indicated.
1234 **(I)** Percentage of cells with separated SPBs upon quiescence exit on YPDA agarose pad (N = 4,
1235 n > 200, left panel). Right: proliferation of WT and *kip3Δshe1Δ* strains in YPDA (OD 600nm as
1236 function of time).
1237 **(J)** Q-nMT bundle length distribution in WT (grey) or *kip3Δshe1Δ* (green) cells with
1238 unseparated SPBs, 240 min after quiescence exit.

1239 **(K)** Actin (red, phalloidin-staining) in WT and *kip3Δshe1Δ* cells expressing mTQZ-TUB1 (green)

1240 at the indicated time upon quiescence exit, bar is 2µm.

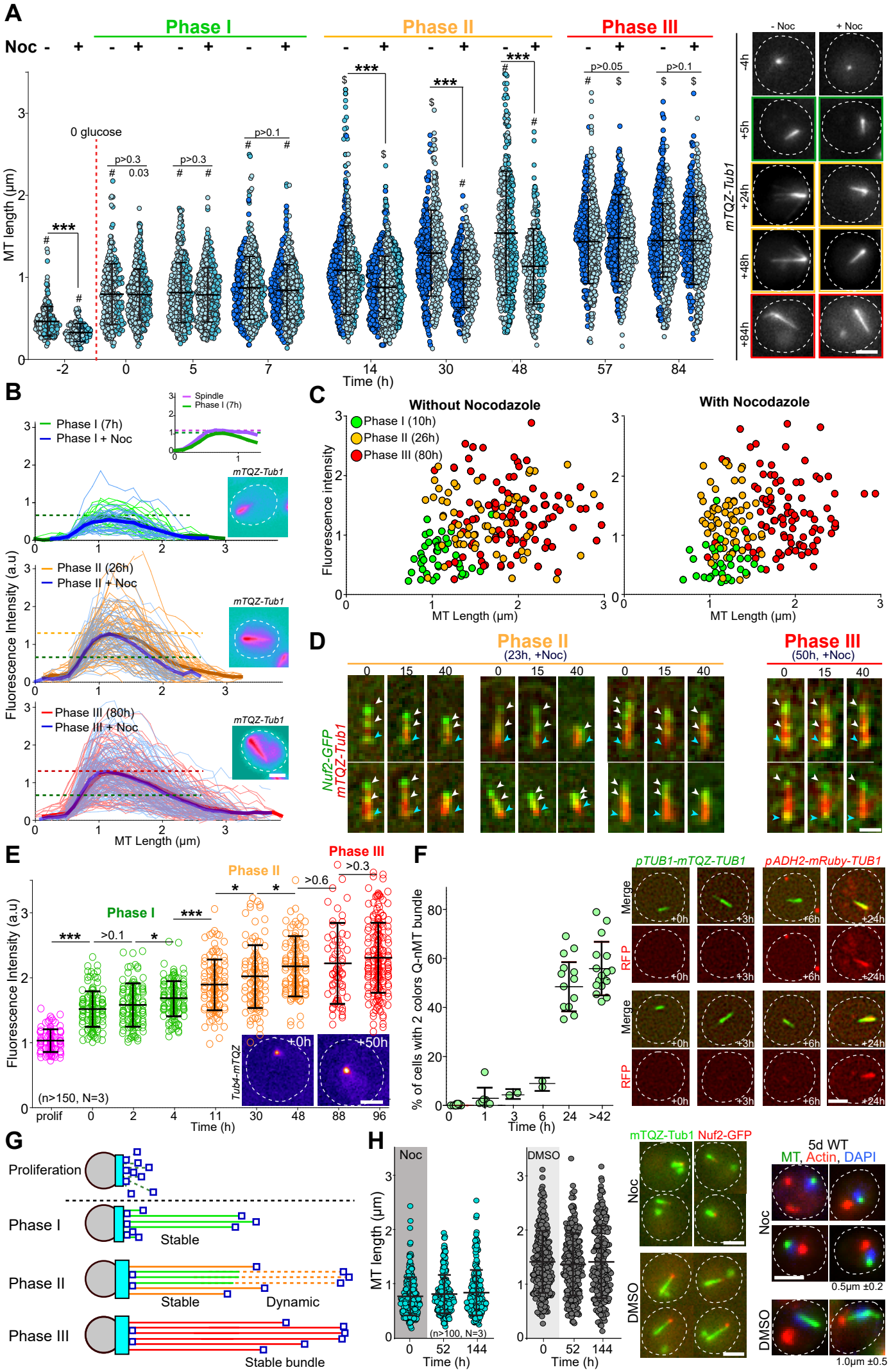
A
Phase I
Phase II
Phase III
Noc - + - + - + - + - + - + - + - + - + - +
MT length (µm)
0 glucose
p>0.3
0.03
p>0.1
p>0.05
***
Time (h)
-2
0
5
7
14
30
48
57
84
- Noc
+ Noc
mTQZ-Tub1
-4h
+5h
+24h
+48h
+84h
B
Phase I (7h)
Phase I + Noc
Spindle
Phase I (7h)
mTQZ-Tub1
Phase II (26h)
Phase II + Noc
Phase III (80h)
Phase III + Noc
Fluorescence Intensity (a.u)
MT Length (µm)
C
Without Nocodazole
With Nocodazole
Phase I (10h)
Phase II (26h)
Phase III (80h)
Fluorescence intensity
MT Length (µm)
D
Phase II
(23h, +Noc)
Phase III
(50h, +Noc)
0
15
40
Nuf2-GFP
mTQZ-Tub1
E
Phase I
Phase II
Phase III
Fluorescence Intensity (a.u)
>0.1
>0.3
>0.6
(n>150, N=3)
Tub4-mTQZ
+0h
+50h
prolif
Time (h)
F
% of cells with 2 colors Q-nMT bundle
Time (h)
pTUB1-mTQZ-TUB1
pADH2-mRuby-TUB1
Merge
RFP
+0h
+3h
+6h
+24h
G
Proliferation
Phase I
Stable
Phase II
Stable
Dynamic
Phase III
Stable bundle
H
Noc
DMSO
MT length (µm)
(n>100, N=3)
Time (h)
mTQZ-Tub1 Nuf2-GFP
5d WT
MT, Actin, DAPI
0.5µm ±0.2
1.0µm ±0.5

Figure 1

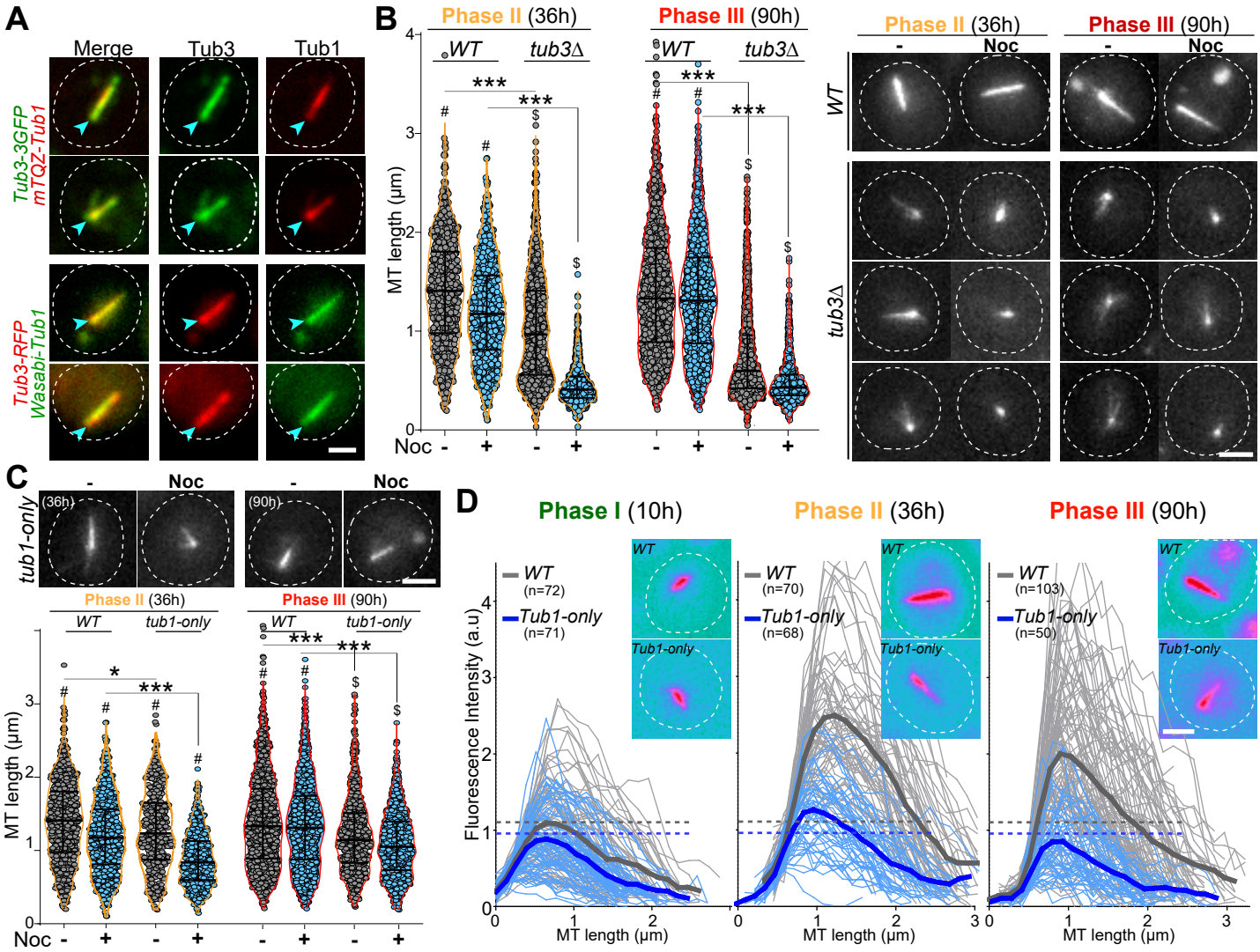
A
Merge
Tub3
Tub1
Tub3-3GFP
mTQZ-Tub1
Tub3-RFP
Wasabi-Tub1
B
Phase II (36h)
Phase III (90h)
WT
tub3Δ
MT length (µm)
Noc
Phase II (36h)
Phase III (90h)
Noc
WT
tub3Δ
C
tub1-only
(36h)
(90h)
Noc
Phase II (36h)
Phase III (90h)
WT
tub1-only
MT length (µm)
Noc
D
Phase I (10h)
Phase II (36h)
Phase III (90h)
WT
(n=72)
Tub1-only
(n=71)
(n=70)
(n=68)
(n=103)
(n=50)
Fluorescence Intensity (a.u)
MT length (µm)

Figure 2

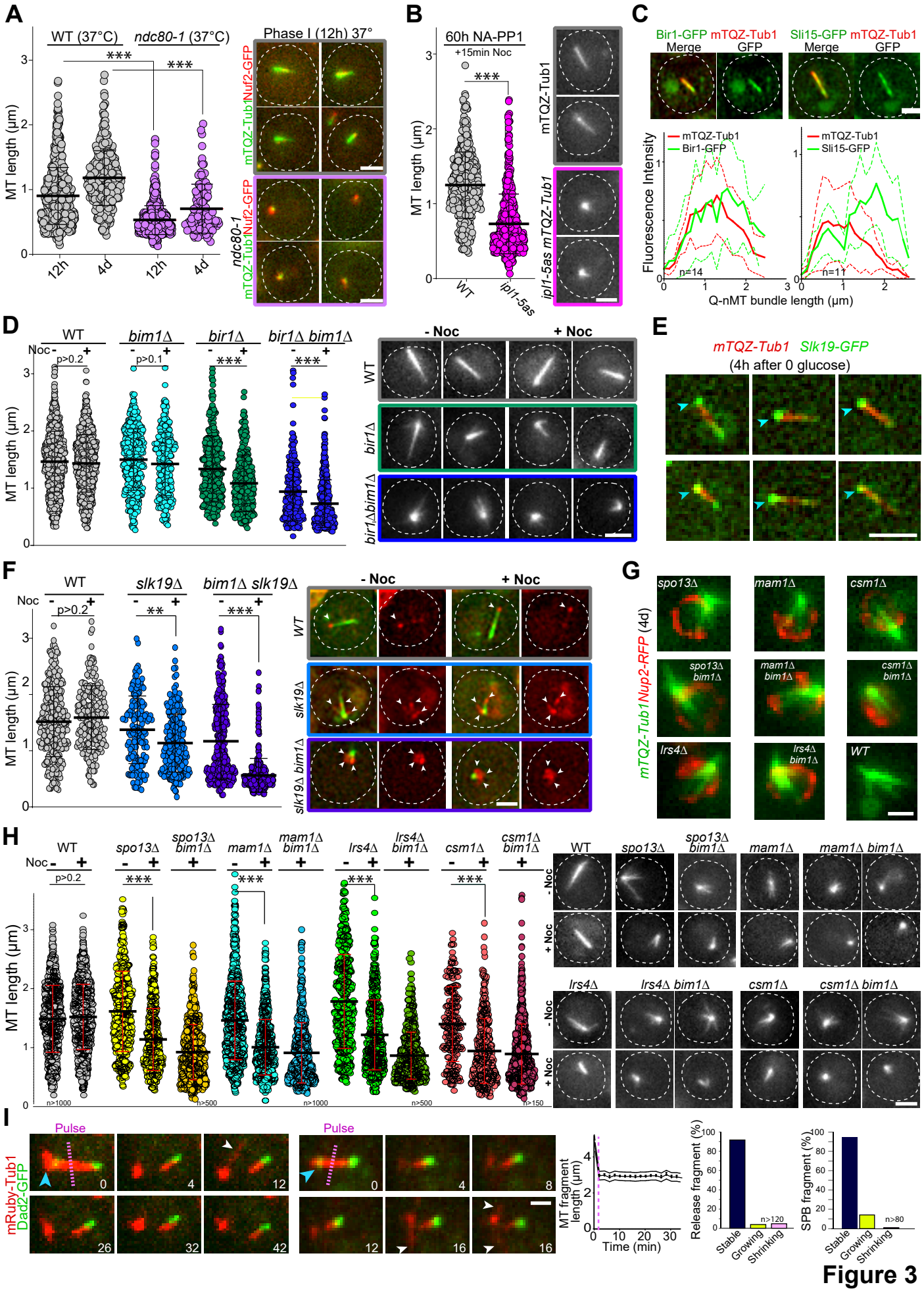
A
WT (37°C)
ndc80-1 (37°C)
Phase I (12h) 37°
MT length (µm)
12h
4d
mTQZ-Tub1Nuf2-GFP
ndc80-1
B
60h NA-PP1
+15min Noc
WT
ipl1-5as
mTQZ-Tub1
ipl1-5as mTQZ-Tub1
C
Bir1-GFP mTQZ-Tub1
Sli15-GFP mTQZ-Tub1
Merge
GFP
Fluorescence Intensity
Q-nMT bundle length (µm)
D
WT
bim1Δ
bir1Δ
bir1Δ bim1Δ
Noc
- Noc
+ Noc
bir1Δbim1Δ
E
mTQZ-Tub1 Slk19-GFP
(4h after 0 glucose)
F
slk19Δ
bim1Δ slk19Δ
slk19Δ bim1Δ
G
spo13Δ
mam1Δ
csm1Δ
spo13Δ bim1Δ
mam1Δ bim1Δ
csm1Δ bim1Δ
lrs4Δ
lrs4Δ bim1Δ
mTQZ-Tub1Nup2-RFP (4d)
H
spo13Δ bim1Δ
mam1Δ bim1Δ
csm1Δ bim1Δ
lrs4Δ bim1Δ
I
Pulse
mRuby-Tub1
Dad2-GFP
MT fragment length (µm)
Time (min)
Release fragment (%)
SPB fragment (%)
Stable
Growing
Shrinking

Figure 3

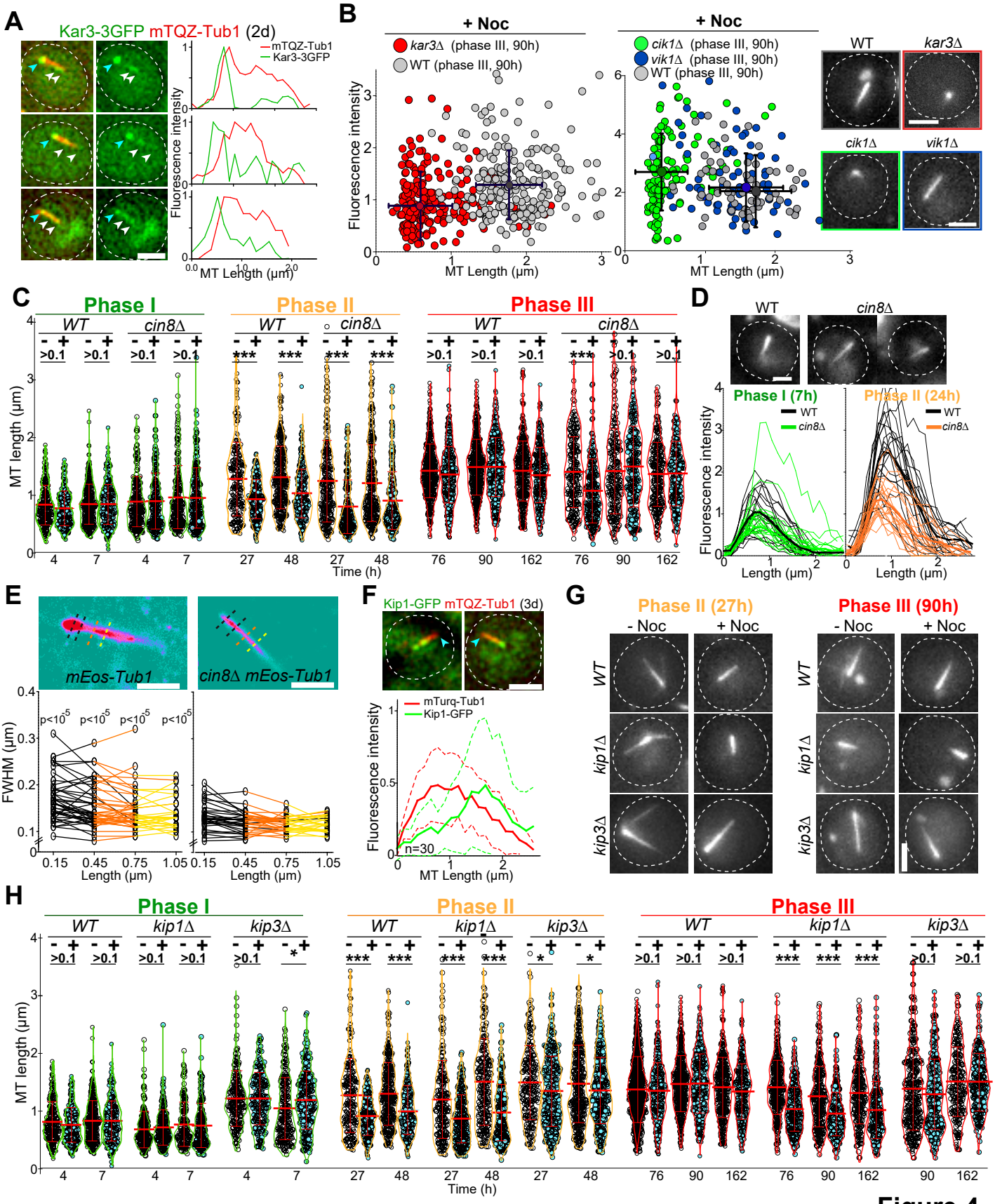
A
Kar3-3GFP mTQZ-Tub1 (2d)
mTQZ-Tub1
Kar3-3GFP
Fluorescence intensity
MT Length (µm)
B
+ Noc
kar3Δ (phase III, 90h)
WT (phase III, 90h)
+ Noc
cik1Δ (phase III, 90h)
vik1Δ (phase III, 90h)
WT (phase III, 90h)
Fluorescence intensity
MT Length (µm)
WT
kar3Δ
cik1Δ
vik1Δ
C
Phase I
Phase II
Phase III
WT
cin8Δ
MT length (µm)
Time (h)
D
WT
cin8Δ
Phase I (7h)
Phase II (24h)
Fluorescence intensity
Length (µm)
E
mEos-Tub1
cin8Δ mEos-Tub1
FWHM (µm)
Length (µm)
F
Kip1-GFP mTQZ-Tub1 (3d)
mTurq-Tub1
Kip1-GFP
Fluorescence intensity
n=30
MT Length (µm)
G
Phase II (27h)
Phase III (90h)
- Noc
+ Noc
WT
kip1Δ
kip3Δ
H
Phase I
Phase II
Phase III
WT
kip1Δ
kip3Δ
MT length (µm)
Time (h)

Figure 4

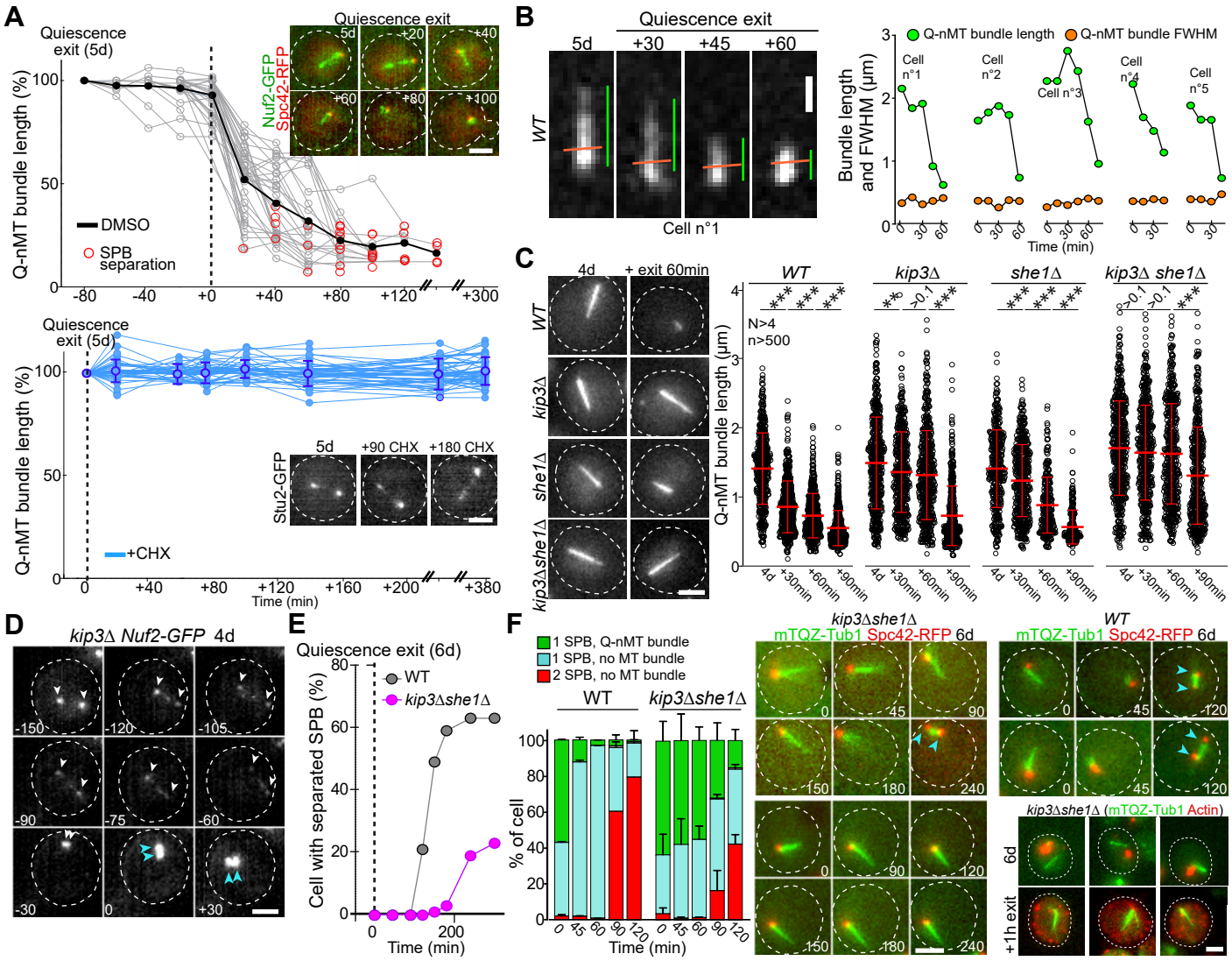
A
Quiescence exit (5d)
Q-nMT bundle length (%)
DMSO
SPB separation
Quiescence exit
Nuf2-GFP Spc42-RFP
5d
+20
+40
+60
+80
+100
+CHX
Stu2-GFP
+90 CHX
+180 CHX
Time (min)
B
Quiescence exit
5d
+30
+45
+60
WT
Cell n°1
Q-nMT bundle length
Q-nMT bundle FWHM
Bundle length and FWHM (µm)
Cell n°1
Cell n°2
Cell n°3
Cell n°4
Cell n°5
C
4d
+ exit 60min
WT
kip3Δ
she1Δ
kip3Δ she1Δ
Q-nMT bundle length (µm)
N>4
n>500
4d
+30min
+60min
+90min
D
kip3Δ Nuf2-GFP 4d
E
Quiescence exit (6d)
Cell with separated SPB (%)
WT
kip3Δshe1Δ
Time (min)
F
1 SPB, Q-nMT bundle
1 SPB, no MT bundle
2 SPB, no MT bundle
% of cell
Time (min)
kip3Δshe1Δ
mTQZ-Tub1 Spc42-RFP 6d
WT
mTQZ-Tub1 Spc42-RFP 6d
kip3Δshe1Δ (mTQZ-Tub1 Actin)
6d
+1h exit

Figure 5

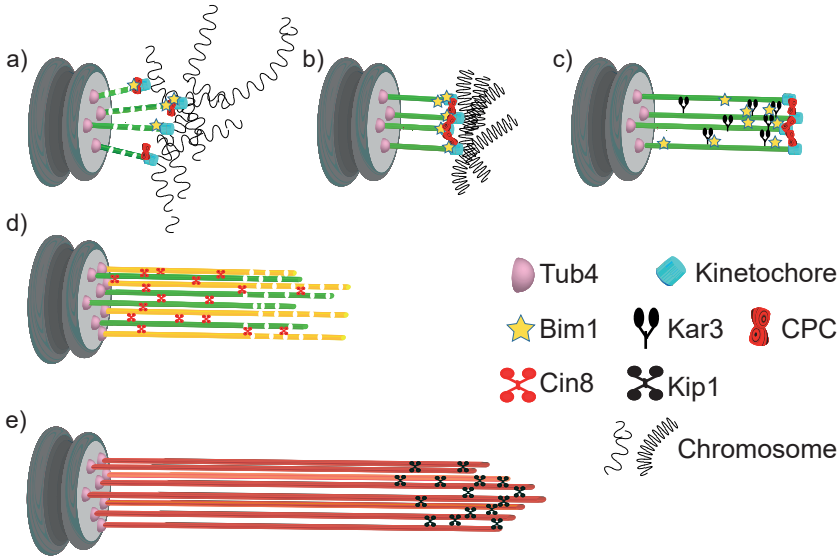

Figure 6